Lawrence Berkeley National Laboratory

Recent Work

Title

IMPROVED BETA-ALUMINA ELECTROLYTES FOR ADVANCED STORAGE BATTERIES PROGRESS REPORT - SEPT. 1980

Permalink

https://escholarship.org/uc/item/5299n84b

Author

Jonghe, L.C. De

Publication Date

1980-09-01

Lawrence Berkeley Laboratory

UNIVERSITY OF CALIFORNIA
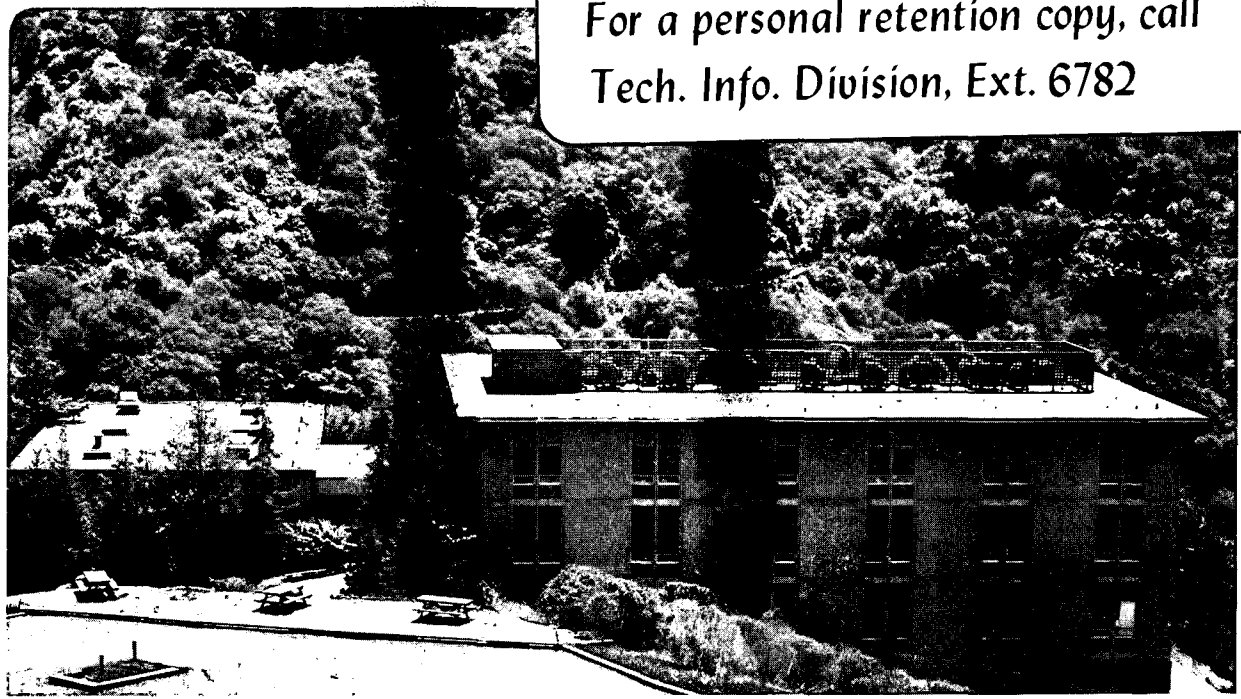
Materials & Molecular Research Division

IMPROVED BETA-ALUMINA ELECTROLYTES FOR
ADVANCED STORAGE BATTERIES
PROGRESS REPORT - SEPTEMBER 1980

Lutgard C. De Jonghe

September 1980

DISCLAIMER

IMPROVED BETA-ALUMINA ELECTROLYTES FOR ADVANCED STORAGE BATTERIES

Progress Report - September 1980

Prepared by

Lutgard C. De Jonghe
Principal Investigator

Materials and Molecular Research Division
Lawrence Berkeley Laboratory
University of California
Berkeley, CA 94720

ABSTRACT

Investigations on the factors determining the mechanisms of electrochemical failure initiation and propagation of polycrystalline sodium beta and beta" alumina are reported. The investigations have led to the distinction between two modes of failure. Mode I failure involves a cathodic plating of sodium into a pre-existing crack. Mode II degradation involves the internal precipitation of sodium.

The Mode I initiation current density thresholds were determined using acoustic emission detection. Experiments below and above the melting point of sodium have been carried out. The results are reported in the form of Weibull failure probability plots. Below the melting point of sodium, the average current density threshold for initiation of Mode I failure depended on temperature, with an activation energy of about 4 kcal/mol. At 350°C, it was found that a significant grain size dependence existed, in which large grained material exhibited lower average critical current density thresholds for Mode I initiation than fine grained material.

Evidence was also found for internal precipitation of sodium, Mode II degradation. It is indicated that this Mode II degradation probably results from charge transfer through a gradient in transport number ratios. These gradients are introduced by the chemical reduction of the beta aluminas when in contact with molten sodium. The chemical reduction has a discoloration associated with it. The nature of this chemical coloration has been examined and is reported. Chemical coloration involves the introduction of oxygen vacancies into the ceramic electrolyte, compensated by electrons.

A method is reported that is capable of revealing electrode current density inhomogeneity with the resolution of about 1 micrometer.

A method was also developed for revealing the presence of fine, sodium-filled cracks. This method involves staining of the electrolyte by immersion in silver nitrate solution.

ACKNOWLEDGEMENTS

CONTENTS

ILLUSTRATIONS

TABLES

SUMMARY

The approach taken in our investigations has been to examine carefully electrolytes tested in-cell by battery developers, and to perform high current density testing that leads to rapid failure on unused, state-of-the-art electrolytes. The materials science methodology has been followed in which detailed microstructural examinations are an integral and important part of the analysis. This has been coupled with what is currently understood about electrolyte degradation, and has led us to a partial understanding of a new "Mode II" degradation. The previously studied "Mode I" degradation involves the rapid propagation of a small, pre-existing surface flaw at some critical electrode current density. One of the problems with the explanation of this experimentally well documented electrolyte failure is that detailed modeling, based on fracture mechanics, leads to current density thresholds that differ by as much as a factor of 10^5 from the actually observed ones. Our examinations of the degradation has led to formulating a failure mechanism, "Mode II," in which a non-negligible electron/ion transport number gradient plays an essential role. Such a gradient may lead to internal sodium metal formation and accompanying microfracture upon charge transfer through it. Similarly, local electronic effects at the tip of the Mode I cracks should very significantly lower the critical current density thresholds that were calculated with fracture mechanics. Our considerations on Mode II have led to the identification of the following parameters that should adversely contribute to cell lifetimes:

    1.   Applied charging voltages in excess of about three volts.
    2.   Increased electrolyte thickness.
    3.   Increases in electrolyte resistance.
    4.   Polarization at the sulfur/electrolyte interface.

Progress was also made in the detection of the onset of Mode I failure during accelerated laboratory sodium/sodium cell tests. Acoustic emission monitoring was found to be the most sensitive detection method. A potentially significant observation was that a wide scatter was found for the critical current densities

initiating Mode I failure. The Weibull statistics parameters range between 1 and 5 for our set of tests.

The nature of the chemical darkening that occurs when beta or beta" aluminas are in contact with molten sodium was examined in detail. It could be shown that the sodium electrode partly reduces the electrolyte by removal of oxygen. While this process itself does not directly cause degradation of the electrolyte, it introduces the electronic/ionic transport number gradient that makes the Mode II degradation possible.

UNRESOLVED ISSUES

The scatter in the Mode I degradation is an issue that needs considerably more attention. It will be necessary to establish if such a scatter is indeed a fundamental aspect of Mode I failure of electrolytes prepared and handled with the usual care. A wide statistical scatter would complicate the reliable operation of battery assemblies containing large numbers of cells.

At present, little is known about the contribution of electrode contamination to electrolyte cycling life. A lot of work remains to be done here, so that permissible container and seal corrosion rates may be established.

Another significant observation was a detection of some degradation at the sulfur side of the in-cell tested electrolytes. This degradation, manifesting itself as small cracks, was found to be associated with the "imprinting" of the graphite felt on the electrolyte surface. The nature and cause of this degradation is quite unclear at present and remains as a future topic for investigation.

Section 1

INTRODUCTION

BACKGROUND AND OBJECTIVES

Beta batteries, using sodium-beta" alumina solid electrolytes as an ion permeable separator between molten sodium metal and sodium polysulphide storage electrodes, continue to be technologically and economically promising systems for load leveling and for verhicle propulsion. Vigorous research and development programs are underway world-wide. While significant progress is being made towards developing reliable systems, a number of fundamental factors relating to durability remain poorly understood. A determining factor in the ultimate viability of the system is the lifetime of the solid electrolyte upon cell cycling. The factors that correlate with lifetime have been difficult to establish. One of the problems is that a variety of electrolyte degradation processes may take place simultaneously, and that actual cell lifetime testing can take up to several years per cell. Systematic cell lifetime tests are therefore very costly.

The objective of this research project is to determine the mechanisms of electrochemical failure initiation and propagation for polycrystalline Na-β" alumina tubes used for the advanced storage beta batteries that are currently under development. Of particular interest is the definition of those factors that contribute adversely to slow, in-cell electrolyte degradation or to rapid failure.

Section 2

EXPERIMENTAL

MATERIALS

The electrolytes that were studied were prepared to a specific grain size by Ceramatec, Inc., Salt Lake City, Utah. The electrolyte composition was: 8.85 wt % Na_2O; 0.75 wt % Li_2O; balance Al_2O_3. As appropriate, bars, disks or tubes were used for the experiments. The electrolytes tubes were stored in an oxygen and water free (<1 ppm) glove box (Vacuum Atmospheres Company, Los Angeles, California. HE 93-2 Dry lab with MO40-1 Inert Gas Purifier).

The sodium was S-135, Certified ACS from Fisher Scientific Company, Santa Clara, California.

Large single crystals of sodium-beta alumina were obtained from Union Carbide, Linde Division, San Diego, California. These crystals tended to cleave along the basal planes. Most of the spontaneous cleavage cracks could be healed by annealing the crystals at 1600°C in air for 2 hours, packed in coarse sodium-β alumina powder to avoid soda loss.

TRANSMISSION ELECTRON MICROSCOPY

Electron transparent foil were prepared by ion milling of thin sections of electrolytes. A Siemens 102, 100 kV instrument was used for regular or high resolution microstructural characterization. When foils thicker than about 2000Å were necessary to avoid some artifacts, a Hitachi 650 kV transmission electron microscope was used. This made it possible to examine foils up to a thickness of about 3 μm.

Analytical transmission electron microscopy was performed on some degraded electrolytes with a Philips 400A scanning transmission electron microscope. In

this method, an electron beam with a diameter of about 0.2 μm is focussed on the area of interest in the foil. The resulting X-ray emission is analyzed with an energy dispersive X-ray spectrometer permitting the identification of elements with $z \geq 11$ and the estimation of their relative amounts.

ACOUSTIC EMISSIONS DETECTION

When electrolytes fail by initiation and propagation of cracks, stress waves are generated as a result of the stored energy release. These stress waves or acoustic emissions can be monitored by a sensitive transducer, and either the cumulative acoustic events or the number of acoustic events per second can be recorded. In our experiments the increase in count rate appeared to be the clearest indication of the onset of acoustic activity. A similar method was used recently by Worrell and Redfern (1).

An acoustic emission detection system manufactured by the Acoustic Emissions Technology Corporation, Sacramento, California, was used. An acoustic tranducer was coupled to the specimen via an alumina or glass waveguide rod. the signals were filtered and counted by a Model 204A detector. It was important to insure excellent contact at the various mechanical interfaces in the system, since the acoustic emissions that accompanied the onset of breakdown were not very pronounced. Strict precautions needed to be taken to eliminate interference from other sources such as noisy electrical contacts or noisy mechanical friction contacts. The method was only useful for the detection of the onset of rapid breakdown.

SODIUM/SODIUM TEST CELLS

Sodium/sodium cells were constructed using sodium-beta" solid electrolytes. Tubes of the electrolytes with a wall thickness of 1.5 mm, and a diameter of 19 mm, were cut into rings, under kerosene. The rings were approximately 15 mm high. These rings were sealed to a small disk and to a tube of alumina with a sealing glass (Ownens-Illinois IN-3 package sealant). Prior to welding, the electrolyte tubes were carefully washed in ethanol and acetone, and heated for 30 min to about 700°C to drive off all organic matter and water. For the welding the outside of the electrolyte rings were covered with the sealing glass, except for a small area of about 0.2 cm^2 left exposed for current flow. The
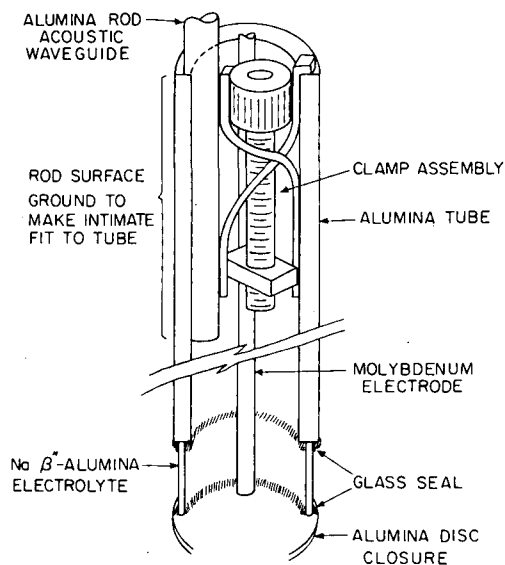
Figure 1. Sodium/Sodium Test Cell

cells were then introduced into the glove box and filled with sodium. A sketch
of the cell is shown in Figure 1.

The sodium/sodium cells was then brought up to temperature and cycled for a few
hours at a very low current density. This cycling at low current densities,
typically on the order of 10 to 20 mA/cm^2 served to "condition" the electro-
lyte interfaces. After such treatment, wetting of the electrolyte by Na was
always complete. Then, increasing current was passed through the cells until
failure. The current density was increased from 0 to as much as 15 A/cm^2 at a
controlled rate, keeping the current direction constant. During the experiments
acoustic emissions were monitored, and the current–voltage vs. time behavior was
recorded.

The current increase rate was such that the cells failed in one cycle, so that
the external exposed area of the electrolyte ring acted only as a sodium exit
surface after the initial, low current density conditioning cycling. To examine
the possible points of origin of failure in relation to microstructure, some
large grain Na-β" alumina rings were polished on the outside wall prior to
assembling of the Na/Na cells. This permitted examining the cycled electrolyte

surfaces for local degradation such as grain boundary attack.

DEGRADATION INITIATION TESTS BELOW 100°C

Onset of rapid electrolytic failure was studied on polycrystalline sodium-β″ alumina. The experimental set-up is sketched in Figure 2. Bar shaped samples were immersed in a liquid mercury-sodium amalgam anode. The cathode was a gold layer deposited by evaporation or a silver layer painted on the end of the sample. A silica waveguide was used to couple the acoustic emissions sensor to the specimen. The set-up shown in Figure 2 was enclosed in a temperature controlled chamber and assembled in the glove box. In a typical experiment, samples were held under a low current (about 10 mA/cm^2) above the melting point of sodium, so that the cathode became completely covered with sodium without the initiation of breakdown. The current was interrupted and the specimen was cooled to the test temperature. The current was then increased until breakdown initiation was indicated by a sudden rise in the acoustic emission rate.

DECORATION OF TESTED ELECTROLYTES

When ionic currents are passed through sodium beta aluminas, metal filled cracks may propagate from the cathodic to the anodic surface. The sodium cracks or
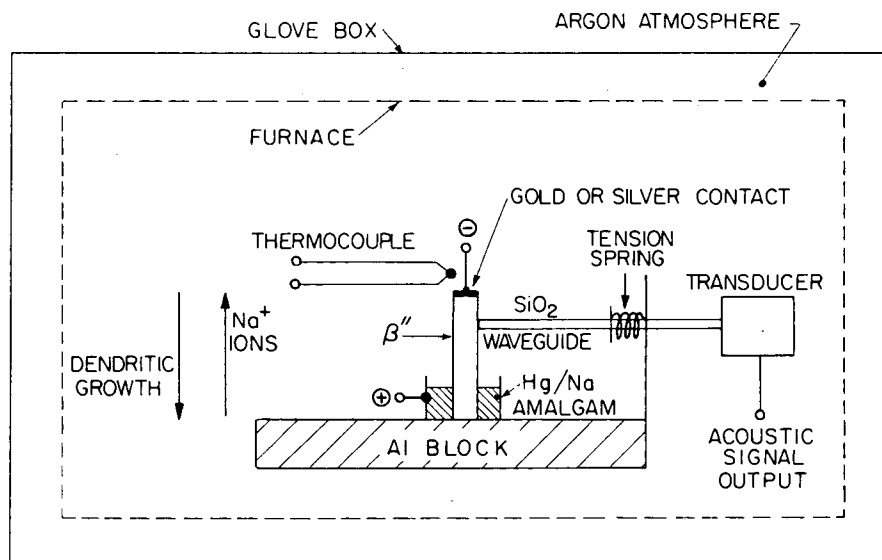
Figure 2. Experimental Set Up for the Low Temperature Failure Experiments

crack networks that have propagated through the sample usually appear optically very diffuse. This is because the polycrystalline electrolytes are translucent rather than transparent, and light scattering prevents a clear examination of the metal filled cracks. Where the cracks intersect the surface, reaction with moisture and CO_2 in the ambient atmosphere depletes the sodium locally so that the optical surface detection of cracks is difficult. Crack openings are quite small, so that regular dye penetrants are ineffective. In our chemical decoration method, the samples, before or after polishing, are submerged from five to twenty minutes in an aqueous, one molar solution of silver nitrate kept at about 80°C. The cracks are then decorated with a dark deposit. Presumably, Ag^+ reacts with the NaOH that has formed in the fine cracks. When viewed with crossed polarizers, to reduce surface reflection, the details of the crack network show up clearly. Figure 3 is an example of silver decorated cracks and crack clusters of an anodic surface of a beta" electrolyte that was degraded by current passage below the melting point of sodium. Dense crack clusters as well as other fine cracks can be observed in this micrograph. Our experiments have also indicated that the staining procedure does not alter the optically observable crack patterns in a detectable way. It can, however, not be excluded that additional cracking might be introduced on a scale that is not detectable by optical microscopy. It should be noted that only those flaws are decorated that contained sodium in them. Polishing scratches and mechanically induced cracks appear not to be decorated by the silver staining method. This method may therefore also be useful in distinguishing degradation due to propagation of sodium filled cracks from accidentally induced cracks.
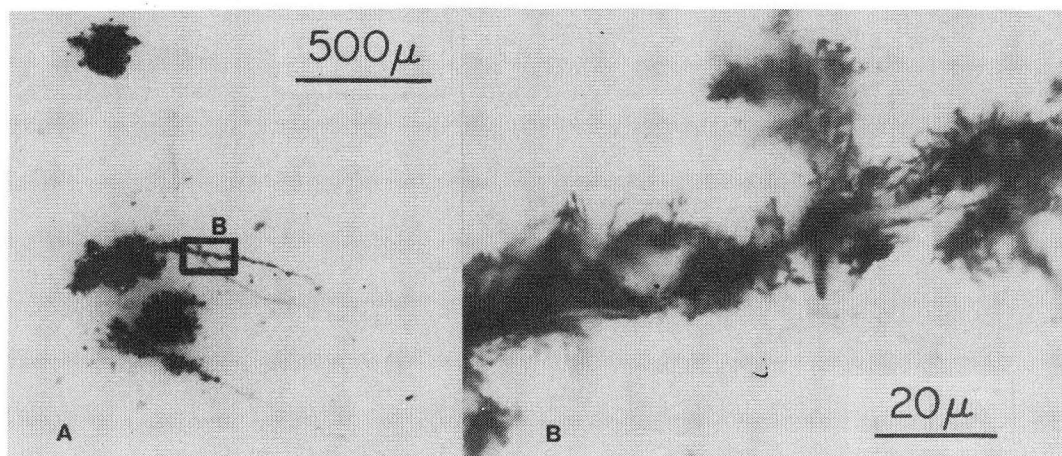
Figure 3. Silver Decorated Cracks

METHOD OF REVEALING LOCAL ELECTRODE CURRENT DENSITIES

Important parameters in the lifetime of the electrolyte used in sodium/ sulfur cells are the electrode current density and the integrated charge passed per unit area of the electrode. It would be useful to minimize electrode current density heterogeneities to delay the initiation of failures. We have found a way of qualitatively revealing the local electrode current density with a resolution of approximately one micron.

A metal salt, dissolved in a water containing medium such as glycerine + 5% H_2O, is used as an anolyte, i.e., a solution bridging an inert anode and the solid electrolyte. When electrolysis is started the sodium ions in the solid electrolyte are transported towards the cathode and are replaced by positive ions from the anolyte. Thus, a certain amount of H_3O^+ ions from the partly dissociated H_2O will be inserted in the electrolyte to replace Na^+ ions. This leaves OH^- ions behind at the anolyte/β'' alumina interface which, at sufficiently high electrode potentials may reduce the anolyte metal ions to metal. For silver nitrate solutions, the following reactions are thought to occur:

$$2 H_2O \rightarrow H_3O^+ + OH^-$$

$$Ag^+ + 2 OH^- \rightarrow Ag(metal) + H_2O + 1/2 O_2 + e^-$$
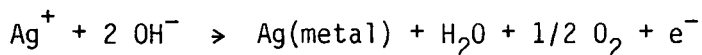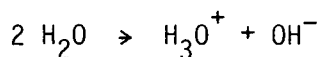
The silver metal deposits on the anolyte/solid electrolyte interface. At sufficiently short times, it is expected that the sample inter-electrode resistance rather than the electrode polarization phenomena determines the local electrode rates. The electrolyte bulk polarization phenomena due to grain boundaries have average relaxation times in the 100 KHz to the MHz range, while electrode processes have relaxation times on the order of a second. For reaction times of one second or less, it is then expected that the amount of deposited silver will be roughly proportional to the local electrode current density of a sample with identical structure but with reversible electrodes. It is also expected, since the electrolyte is a passive ohmic system, that current distributions would be similar for reversible anolyte/electrolyte and for catholyte/electrolyte interfaces.

The method was demonstrated on polycrystalline sodium-beta" alumina with an average grain size of about 300 microns. Prior to its use, the ceramic was stored under anhydrous conditions. The Na-β alumina content was less than 2 vol ; no other phases were detected by X-ray analysis. The electrolyte density was 3.22 g/cm^2 and the electrolyte resistivity was 3.2 ohm-cm.

The experimental set up is sketched in Figure 4. The conditions for obtaining optimum contrast between low and high current density areas were, at room temperature, found to be rather critical. Electrolysis times were about one second and applied electrode potentials were 18 to 20 volts for electrolytes about 5 mm thick.

SCANNING AUGER MICROSCOPY

Some electrolyte specimens were examined in a scanning Auger microscope. The instrument was manufactured by Physical Electronics Industries, Inc., Springfield, New Jersey. The instrument is equipped with a stage that permitted the in-situ fracturing of samples, avoiding carbon contamination. It is capable of mapping the density of such fracture surfaces with a resolution of about 0.3 μm. A difficulty is, however, that mobile ions, such as Na$^+$ in the beta aluminas, migrate during observation so that they cannot be analyzed properly.
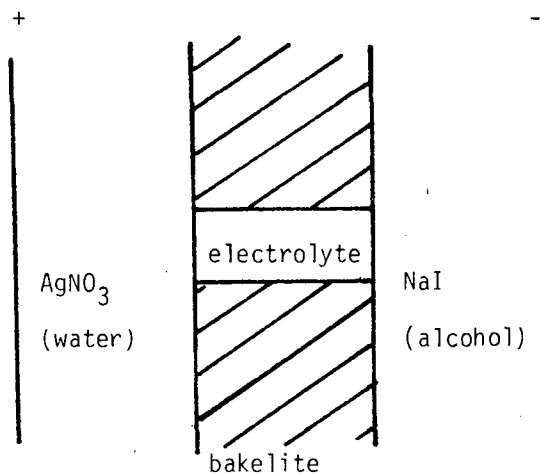
Figure 4. Setup for Electrode
Decoration Experiment

Section 3

EXPERIMENTAL RESULTS

CHARACTERIZATION OF AS-RECEIVED ELECTROLYTES

The tube-shaped solid electrolytes that are used in sodium/sulfur cells can be prepared in a variety of ways. Some users have developed an electrophoretic deposition technique, while others employ tubes that have been fabricated via wet or dry bag isostatic pressing techniques. Each of these fabrication routes may leave peculiar imperfections in the final sintered product. We have examined some of those imperfections in tubes that have been fabricated by an isostatic pressing technique and by an electrophoretic deposition method. In the observations reported below, we have selected those micrographs which showed the imperfections. A significant statistical analysis of the frequency of occurrence of those imperfections has not been made. The fact that the reported imperfections were relatively easy to find in a limited number of cross sections of the ceramic implies that the frequency of occurrence is not negligible. At the same time, it should be stressed that none of the imperfections that were observed in any of the examined electrolytes could in fact be linked to premature ceramic breakdown either in high current density rapid breakdown experiments or in long-time cell testing.

Isostatically Pressed Tubes

A number of tubes, prepared by an isostatic pressing method, were obtained from Ceramatec, Inc., and examined by scanning and optical microscopy. In this method, the powder is compressed by a rubber mold onto a polished steel mandril. From our observations it was immediately apparent that striking differences in surface morphology could be found between the inside and the outside surface of the electrolyte. The general appearance of the outside tube surface, which had been in contact with the rubber mold during isostatic pressing, is shown in Figure 5. The surface appears to be very uneven on a scale of approximately 10 to 15 micrometers. It is thought that this peculiar
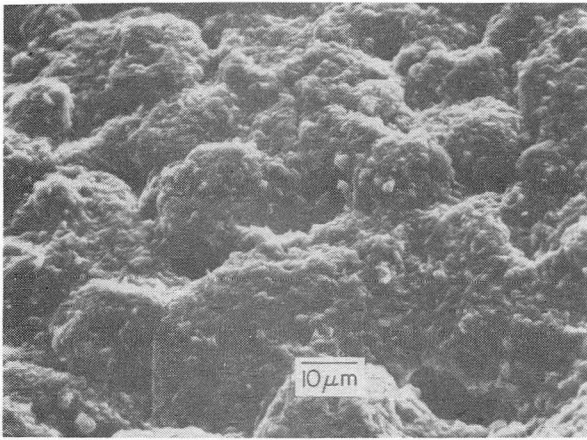
Figure 5. Scanning Electron Micrograph of the Outside Surface of Beta" Tubes Prepared by Isostatic Pressing
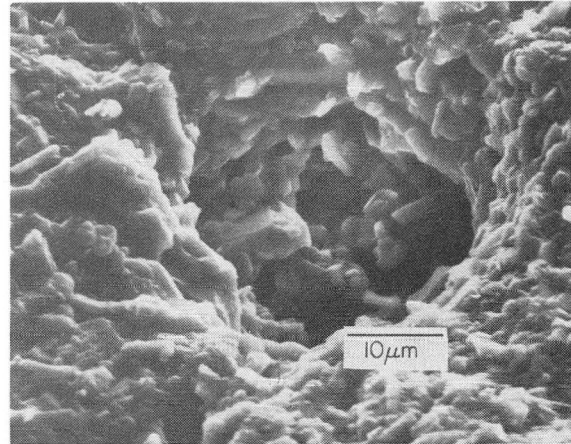
Figure 6. Large Pores in Isostatically Pressed and Sintered Tubes

surface morphology results from the inability of the rubber mold to smooth the granularity of the powder agglomerates, during isostatic compaction. The surface grains appear to be quite small and are generally one micron or less. The largest grains in the surface itself do not exceed 5 micrometers. Occasionally large pores can be found in the surface, as is shown in Figure 6 and Figure 7. The inner surface of the tube that was in contact with the polished steel mandril during pressing, is by contrast smoother on a 10 micrometer scale. Surface unevenness and surface micropores are, however, again
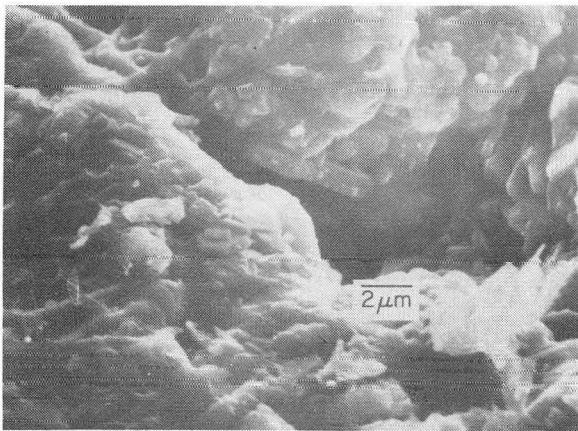
Figure 7. Pore Near the Surface of an Isostatically Pressed and Sintered Tube
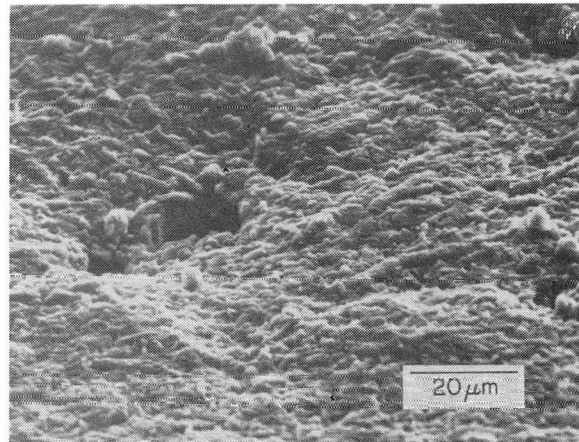
Figure 8. Surface Uneveness and Surface Micropores in Isostatically Pressed and Sintered Tubes

evident here, Figure 8. It is this surface that will be in contact with the sodium in the actual cells.

Interesting differences were also observed between the bulk microstructure of the electrolyte and the near surface structure. These microstructures are shown in Figures 9A and B. In Figure 9A, the bulk microstructure is shown with the usual bimodal grain structure. The largest grains have a long dimension on the order of about 10 micrometers, while the small grains are in the micron or submicron range. Near the surface, Figure 9B, the microstructure appears to be more uniform. Interestingly, curved grains are occasionally observed near the surfaces. Two of such grains have been marked with an arrow in the figure. The origin of such curved grains is not clear. It may be postulated that they could be due to a near surface stress that occurs at some point in the sintering. High temperature compositional changes such as uptake or loss of soda might cause stress gradients that could be sufficient to deform some grains. It is likely that the higher surface layer resistance of the tubes is in fact due to these differences in microstructure shown here.

Pores are also observed inside the solid electrolytes. Two types of pores could be distinguished as shown in Figure 10. The small pores are the micropores while the very large pore is a macropore. These macropores appear to have a rather irregular internal surface structure in which the beta" alumina

10μ
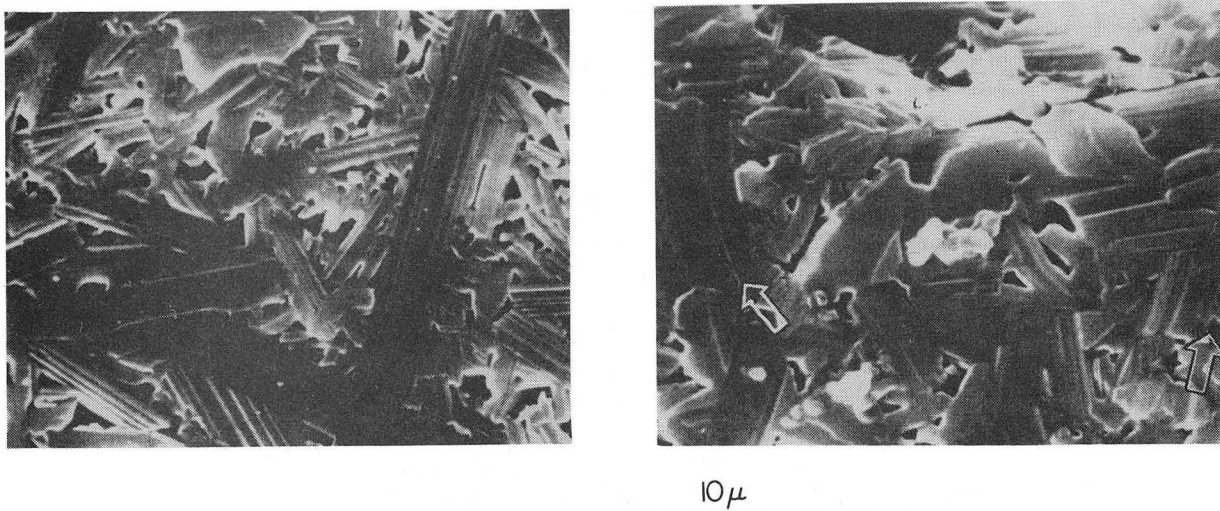
Figure 9. a) Bulk Microstructure Showing Bimodal Grain Structure, b) Curved Grains Near the Surface of the Isostatically Pressed and Sintered Tubes
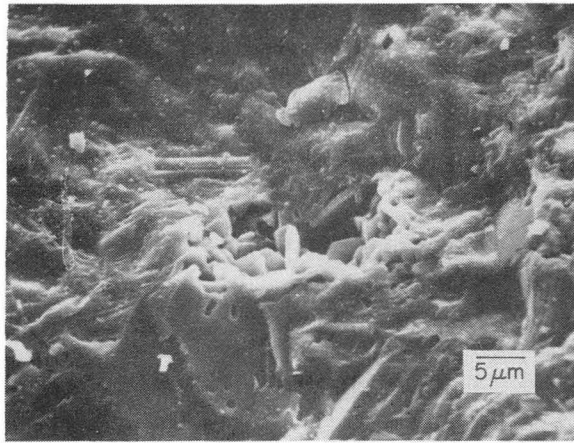
Figure 10.   Small Pores and Macropores
Inside the Solid Electrolyte
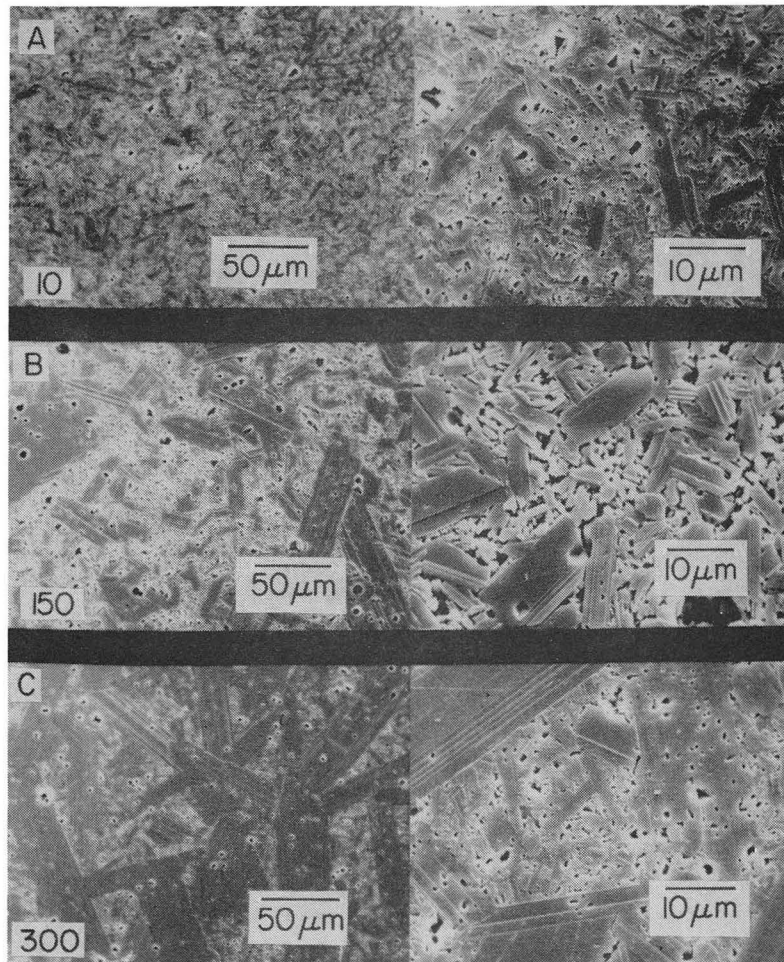
Figure 11.   Comparison of the Microstructures of the Sintered Electrolyte
Used in This Study; Etched in Hot H_3PO_4; Scanning Electron Micrograph

crystallites have been well formed. Since sodium oxide has an appreciable pressure over beta aluminas during sintering, it is likely that this internal recrystallization in the micropores was assisted by a vapor phase transport mechanism.

The microstructures of the electrolytes with nominal grain size of "10," "150," and "300," μm are compared in Figure 11. The grain size distribution appears to be clearly bimodal in the "150" and "300" μm electrolytes. The grain sizes were determined by a random intercept method, in which the number of grain boundaries are counted intercepting a random straight line on a micrograph. The largest grain dimensions were measured directly on individual grains. The results of the measurements and tabulate in Table I.

Table I

MICROSTRUCTURAL DATA

	NOMINAL GRAIN SIZE		
	10	150	300
Overall average grain size	1.1 μm	5.4 μm	5.2 μm
Large grain volume fraction	<0.01 (>10 μm)	0.59 (>10 μm)	0.83 (>10 μm)
Average large grain size	2.4 μm	15 μm	20 μm
Average largest dimension of large grains	14 μm	38 μm	54 μm
Small grain volume fraction	>0.99	0.41	0.17
Average small grain size	0.94 μm	2.8 μm	1.1 μm

Electrophoretically Prepared Tubes

Some tubes prepared by an electrophoretic deposition method were obtained from General Electric Company, Schenectady. The usual surface microstructure and internal grain structure of these tubes are shown in Figure 12. The microstructure of both surfaces is similar and comparable to that of the inside surfaces of the isostatically pressed tubes. Cross sections of these tubes showed two different kinds of pores. This is shown in a low magnification cross section, Figure 13. There are numerous small pores visible with a size of approximately 5 to 10 micrometers. Additionally, there are very large pores that have a diameter up to 70 micrometers. Also, circular type irregularities were occasionally found in these cross sections as shown in Figure 14. Part of
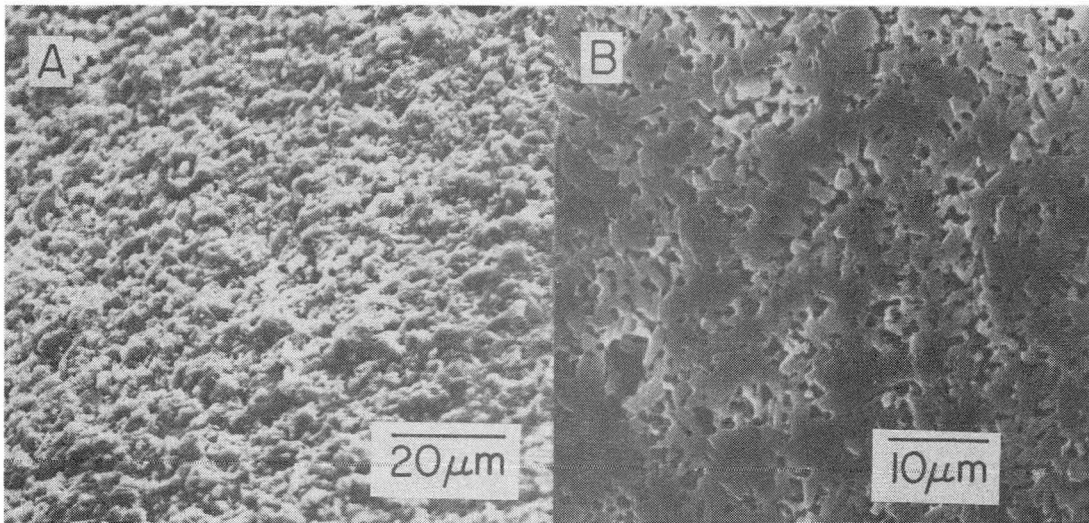
Figure 12. a) Surface Microstructure of Electrophoretically Prepared Tubes, Scanning Electromicrograph. b) Polished, Etched Cross Section of same Tube
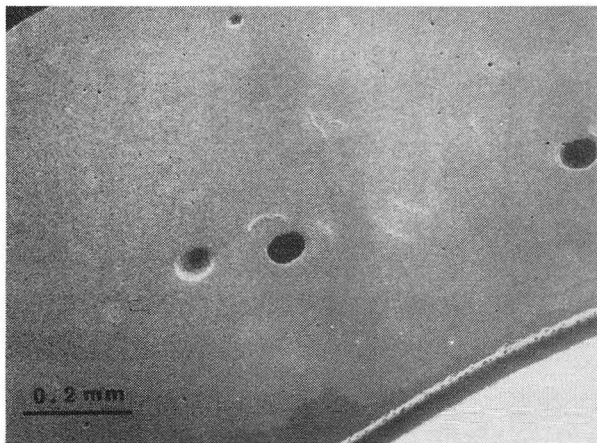
Figure 13. Micro- and Macropores Inside Electrophoretically Prepared Tubes
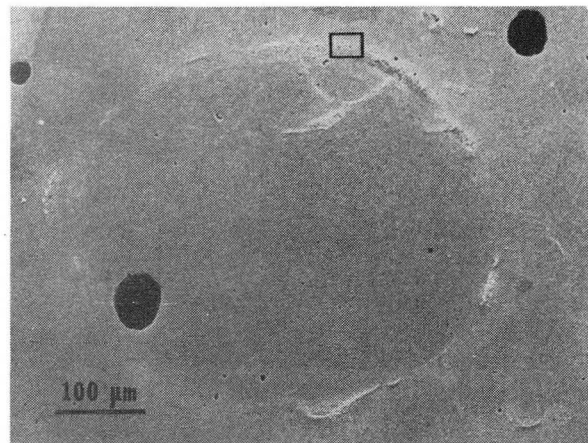
Figure 14. Circular Irregularity in Electrophoretically Prepared Tubes
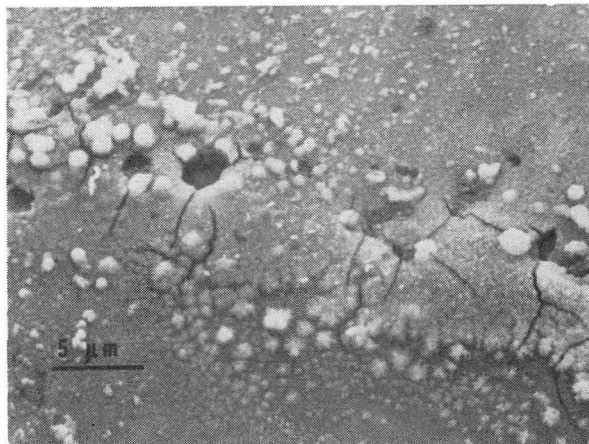
Figure 15. High Magnification of Part of the Circular Irregularity Shown in Figure 14

such an irregularity is shown at a high magnification in Figure 15. These irregularities then seem to consist of clusters of smaller pores as well as small internal cracks. It is believed that such irregularities are introduced in the electrophoretic deposition step. It is at present not known which phenomena could give rise to such large-scale irregularities. Possibly the presence of gas bubbles at the electrolyte/deposit interface during electrophoretic forming might cause defects like this one.

Transmission Electron Microscopy

Electrolytes prepared by Ceramatec and by General Electric were also examined by electron microscopy. Particular attention was paid to the detection of possible grain boundary phases. No grain boundary phases could be detected in the Ceramatec material. An example of a clean grain boundary such as the ones found in the Ceramatec material is shown in Figure 16. The General Electric Material occasionally showed small amounts of a silicate phase at some grain triple junctions.

Local Electrode Current Densities

An example of a silver decorated anodic electrolyte surface is shown in Figure 17. The areas of high silver deposit appear bright in this reflection of optical micrograph. The large circular grain appears dark as would be expected,
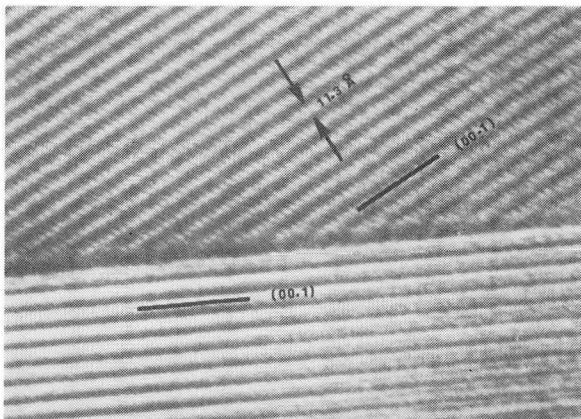
Figure 16. High Resolution Transmission Electron Micrograph of a Clean Grain Boundary in Beta" Alumina
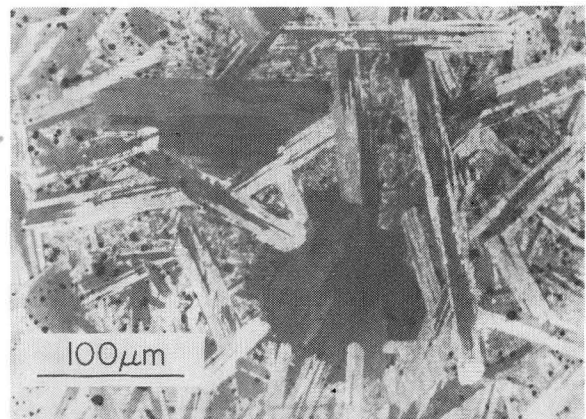
Figure 17. Silver Decorated Anodic Electrolyte Surface

since its conduction planes are approximately parallel to the surface so that no current could enter for geometrical reasons. This leads to local current blocking. Interestingly, grains which are oriented for favorable ionic current injection do not show a uniform current distribution. Apparently different parts of the same grain can carry different current densities. Repeated polishing and redecoration of the same electrolyte surface produced identical patterns, so that it is very unlikely that they could be attributed to local electro-catalytic effects. Instead, the phenomena is thought to be caused by structural differences, such as soda content or syntactic beta-beta" phases, within one grain. The magnitude of the electrode current density in homogeneities was difficult to assess quantitatively. Scanning electron microscopy and energy dispersive x-ray analysis of decorated sample electrode/electrolyte interfaces such as shown in Figure 17 was carried out to estimate the differences in the amount of silver deposited in the different areas of the interface. This analysis revealed that the amount of silver in low and high deposition areas differed by a factor of 2 to 5.

The decoration experiment clearly demonstrated the heterogeneous nature of the beta" alumina electrode interface. It also shows that the high/low current density boundaries are most frequently found where grain boundaries intersect the electrolyte/electrode interface. The general heterogeneity of the electrode current distribution may be seen as being in qualitative agreement with the non-homogeneity of the bulk current distribution as discussed by De Jonghe (2).

MODE I FAILURE INITIATION

A variety of experiments were conducted to find if Mode I degradation (the extension of a pre-existing surface flaw by the Poiseuille pressure due to local cathodic plating of Na) was initiated at some identifiable surface imperfections or particular microstructural configuration. Further, the acoustic emission monitoring was used in experiments below and above the melting point of sodium to establish the electrode current density thresholds at which Mode I degradation would be initiated.

Low Temperature Experiments: T < 100°C

These experiments on Mode I initiation were conducted on the bar shaped Na-beta" alumina electrolytes described in Section 2, and in Figure 2. The breakdown initiation was detected with the acoustic emission method.

To verify the method and the sensitivity, experiments were conducted in which a steady sodium ion current was passed into a beta alumina sample as its temperature was lowered from above 100°C to room temperature. At low current densities on the order of 40 to 50 mA/cm^2 no Mode I degradation should occur above the melting point of sodium. However, as the sodium becomes solid, Mode I degradation gets initiated at extremely low current densities, so that the onset of degradation by the Mode I mechanism should occur at the freezing point of sodium, with its associated acoustic events. The acoustic emissions showed a marked increase in rate at about 2°C below the freezing point of sodium, Figure 18. The usual rapid darkening of the sample that is due to the propagation of sodium-filled cracks appeared at the same time. Samples cooled through freezing point of sodium without the passage of a current showed no change in acoustic activity around the melting point of sodium. These experiments indicated that acoustic emissions monitoring would be used fruitfully to study the initiation of the Mode I breakdown.

In the experiments performed to determine the critical current density thresholds below 100°C, the samples were kept in a temperature controlled enclosure as shown in Figure 2, and the current was increased linearly with time from 0 using a programmable current supply. The current density at which the
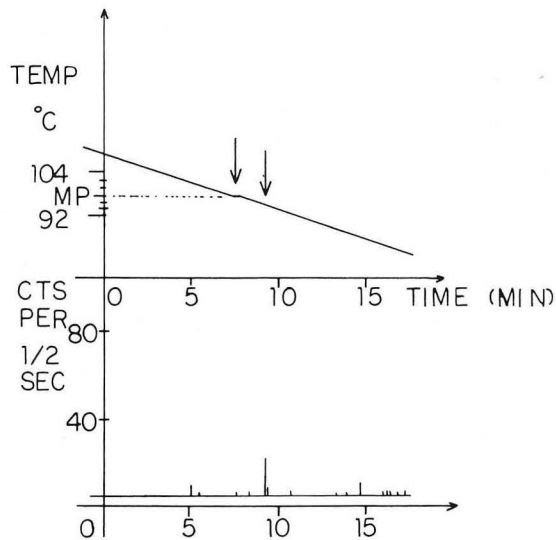
Figure 18. Increased Acoustic Emission
Observed Near the Freezing Point of Sodium

acoustic emission rate suddenly increased above background was taken as the critical current density for initiation of Mode I failure. An example is shown in Figure 19.

Experiments were performed on the three different nominal grain size beta" alumina materials, "10," "150," and "300" µm, described in Table I and shown in Figure 11, and at three different temperatures: 33°C, 65°C and 86°C. The cathode materials were either evaporated gold, silver conductive paint, or fired-on silver paste, but each behaved similarly.

If the critical current density for crack propagation is determined by the presence of a distribution of flaws it will be related to the largest pre-existing flaw in the cathode surface of the ceramic. Assuming there is a
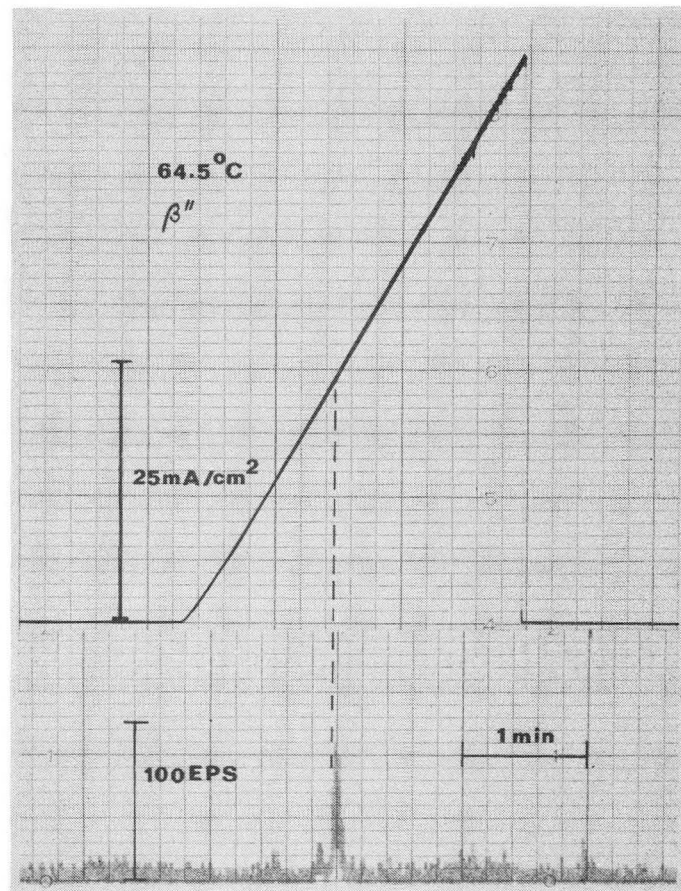
Figure 19. Example of a Determination of the Critical Current Density for the Initiation of Mode I Failure below 100°C

corresponding distribution of critical current densities, the Mode I failure initiation can be described using Weibull statistics. The critical current density distribution for flaws in the cathode surface is analogous to the distribution of flaw strengths in the volume, V, of a brittle solid. The standard treatment of the latter using Weibull statistics (3) gives the survival probability, P_s, as

$$P_s = 1 - P_f = \exp[-V(\sigma - \sigma_u)/\sigma_0)^m]$$

where P_f is the failure probability, σ is the uniform applied stress and σ_u, σ_0, and m are material constants. By analogy, the distribution of critical current densities can be represented by

$$P_s = \exp(-A((j - j_u)/j_0)^m)$$

where A is the cathode area which contains the initial flaws, j is the macroscopic current density, and j_u, j_0 and m are materials parameters. Experimental data can be plotted as $\ln \ln(1/P_s)$ vs $\ln(j - j_u)$. The plotting can be simplified by using a two-parameter Weibull distribution, with $j_u = 0$, where j_u is the current density below which the failure probability is zero. The normalizing current density, j_0, has no particular physical significance, while m, the Weibull modulus, obtained from the slope of $\ln \ln P_s$ vs $\ln(j - j_u)$, characterizes the variability of the critical current density. Large values of m indicate low variability, with m values of 5–20 common for the strength of uniform ceramics. The failure probability, P_f, is obtained from a set of N test data by ranking the results in order of increasing critical current density. The failure probability at a given critical current density is then $i/(N + 1)$, where i is the index of the data point in the ranked series.

The data were plotted in different ways: in the first graphs, Figure 20a–c, the data are plotted at constant temperatures for different grain sizes; in a second graph, Figure 21, the data were plotted disregarding the differences in grain size. The data in Figure 20 appear to correlate with the average grain size of the small grains, although the correlation is weak, and the number of tests carried out was not sufficient to permit establishing this correlation with confidence. Nevertheless, if is felt that this indication of a correlation cannot be disregarded. These initial indications of a correlation with the
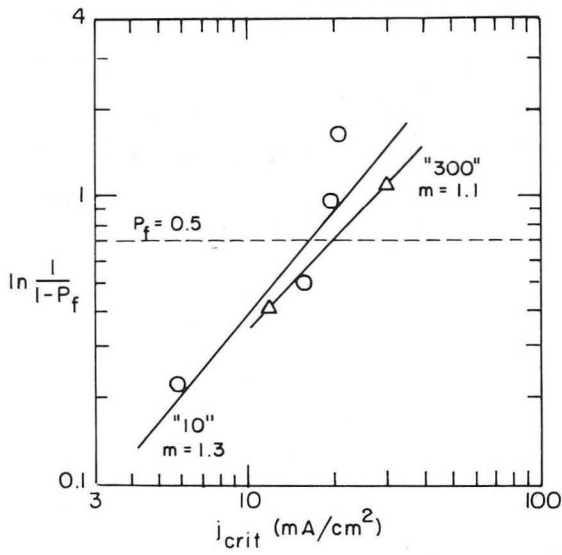
(a)
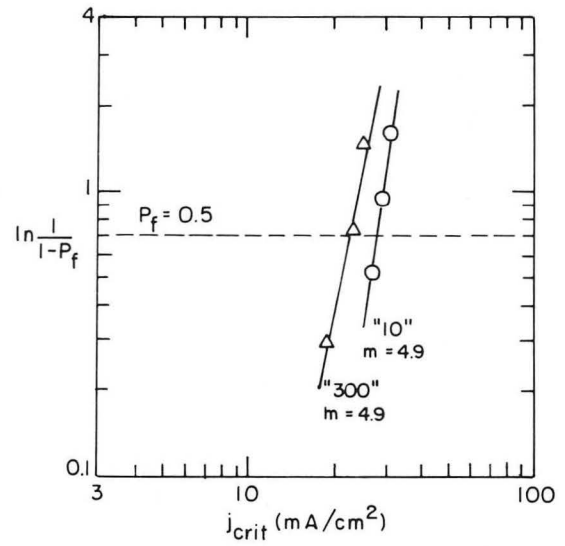
(b)
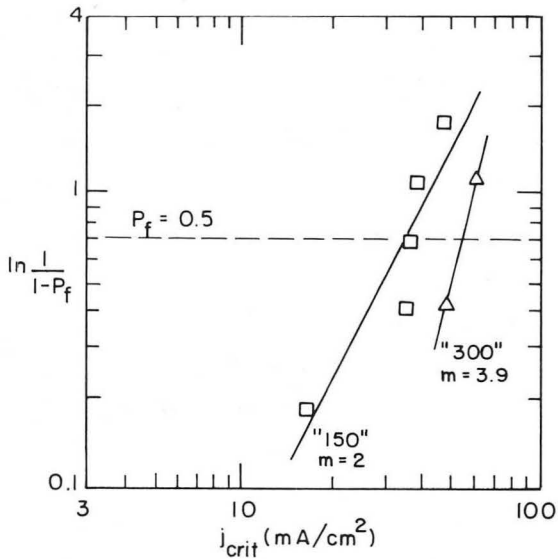
(c)
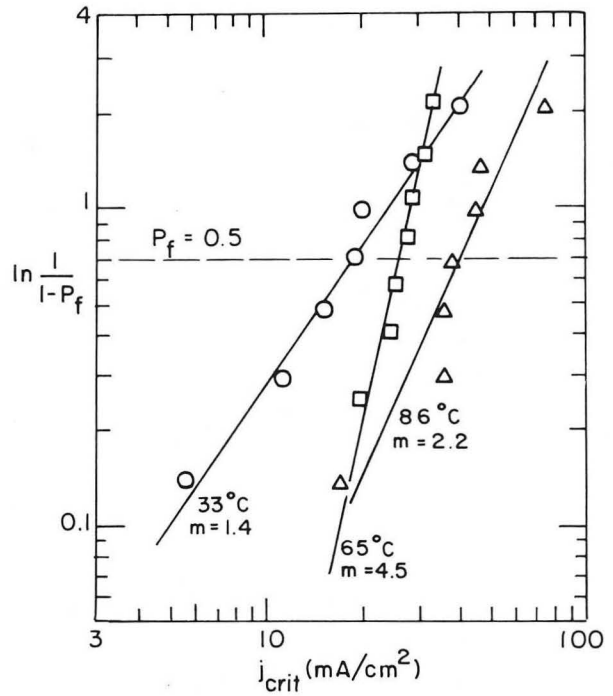
Figure 20. Weibull Plot of Critical
Current Densities, Depending on Grain
Size and Temperature
    (a) 33°C, (b) 65°C, (c) 86°C.

Figure 21. Weibull Plots of
Critical Current Densities
Depending on Temperature,
Disregarding Grain Size
Differences

small grain size fraction may be significant since they are in disagreement with the correlations found above the melting point of sodium (see later in this report). The weak correlation between grain size and critical current density permitted an analysis of the temperature dependence of the current density threshold shown in Figure 21. Here it is seen that the average current density threshold for initiation of Mode I failure increases with increasing temperature, Figure 22. The activation energy is approximately 4 kcal/mole. Interestingly, this is near the value of the activation energy for the ionic resistivity. This suggests that, in fact, the breakdown by Mode I may be dependent on the applied voltage, as well as on the current density, since the applied voltage has to increase to maintain the same current densities at decreasing temperatures.

Although the set of data was not sufficiently large, a potentially important observation is that the Weibull statistical parameter, m, ranges between 1 and 5 for the constant temperature statistical plots. While continued extensive testing is necessary, the results point out that the critical current density for initiation of Mode I may have an intrinsically large scatter.
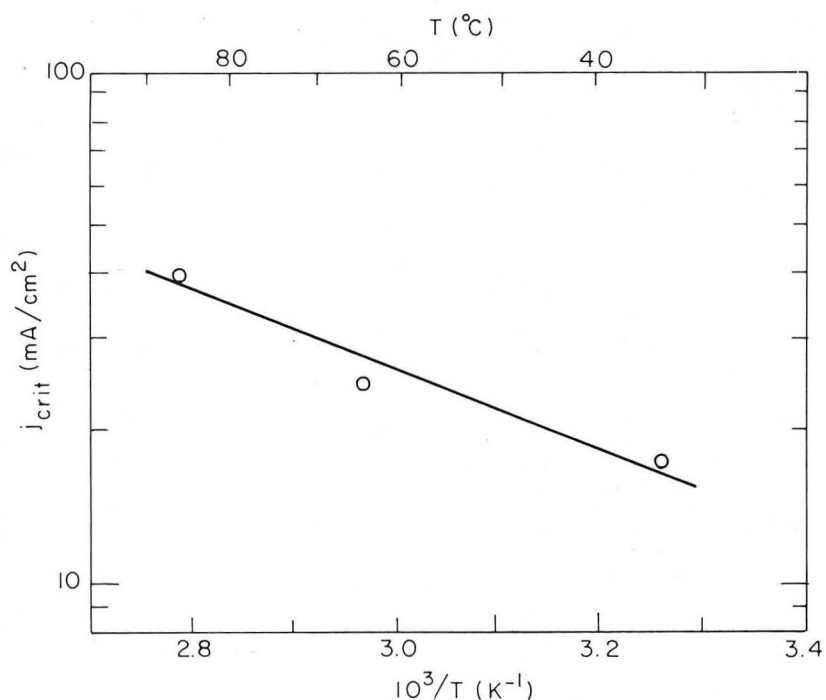
Figure 22. Arrhenius plots of the critical current densities below 100°C. The activation energy is approximately 4 kcal/mole

High Temperature Experiment: T = 350°C

A limited set of tests, using acoustic emission monitoring, were performed on electrolytes in Na/Na cells at 300 to 350°C. A total of about 50 cells were tested.

For some cells, the sodium entrance side appeared to have been attacked. Two of these cells are shown in Figure 23 both in a low magnification optical view and in an SEM micrograph of the surface detail in each case. Cell 90530 had been subjected to 254.7 A hr/cm^2 of charge transfer, while cell 91002 had been subjected to 33 A hr/cm^2. In the SEM micrograph, both of the sodium entrance surfaces are seen to have been attacked. The surface of 90530 is almost sponge-like in appearance.
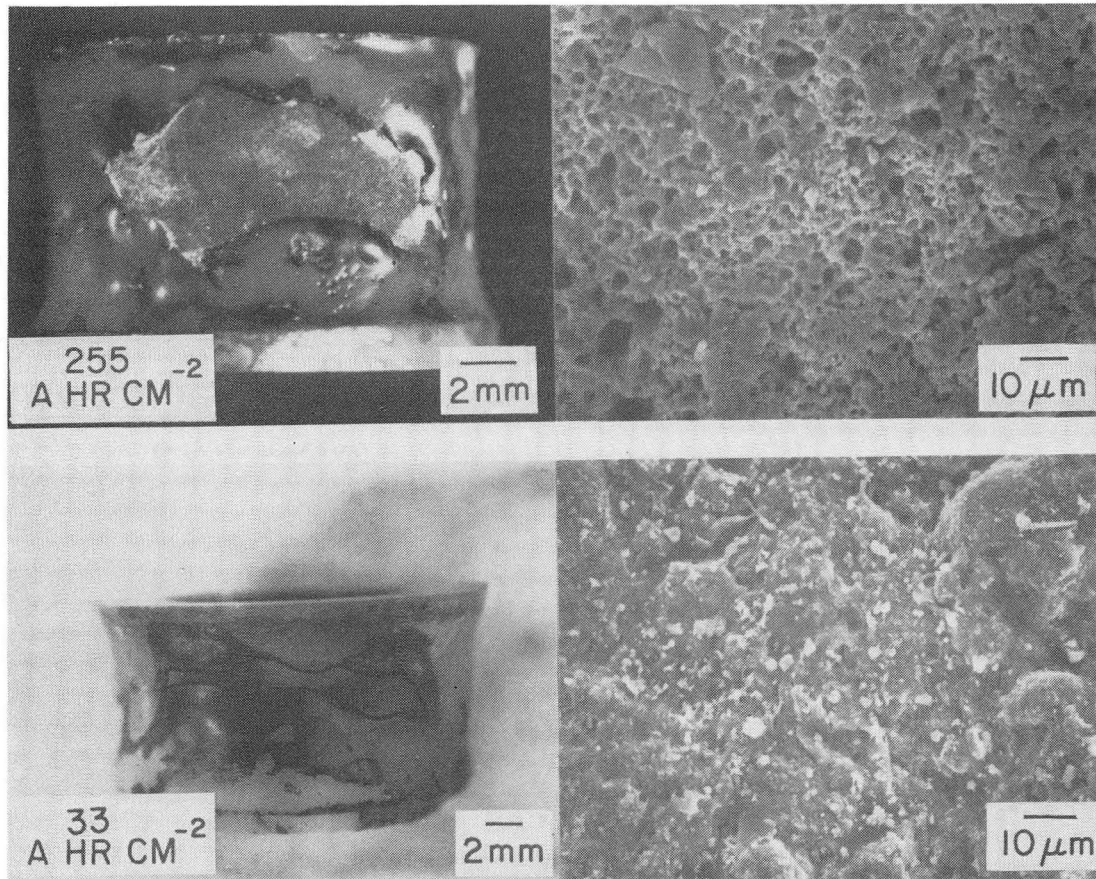
Figure 23. Attack on the sodium entrance surface of sodium/sodium cells for which significant polarization was observed. Cell 90530 has been subjected to 255 Ahr/cm^2, cell 91002 has been subjected to 33 Ahr/cm^2 (Active area of cell is outlined in black).

The reported absence of evidence for stress corrosion of beta aluminas by molten sodium ($\underline{4}$) appears to rule out corrosion as a likely cause and it is therefore thought that the observed surface attack may have been produced by electrical discharge through some polarization layer developed on the Na/electrolyte interface of the sample. The exact conditions under which this type of degradation occurs are not well known at present, but appear in general to be associated with noticeable polarization in the later stages of the cell's life. Considerable acoustic activity was also observed during the strong polarization stages as one would expect if a dielectric type discharge was occurring at this interface during electrolysis. It has been reported that interface polarization is more likely to occur for Na-beta" than for beta aluminas. This was attributed to the greater affinity for water of beta" aluminas. If this electrolyte is exposed to air a monolayer or more of water is immediately adsorbed. When interface polarization develops in beta batteries or the Na-beta" alumina electrolyte, it has been reported that the electrolyte inevitably fails after an additional charge transfer of less than 200 A hr/cm^2, and that the electrolyte surface appears black and crumbly ($\underline{5}$). We believe this phenomenon is related to the one found in our Na/Na cells, which had been subjected to charging voltages of as much as 20 V. However, interface polarization was found to be only significant in our Na/Na tests when the cells were subjected to a steady current density increase in excess of 2 mA/cm^{2}sec. The actual cause of polarization in our cells has, at present, not been determined. It is possible that oxygen contamination of the glove box atmosphere may have led to eventual precipitation of sodium oxides on the electrode/electrolyte interface. Such deposition would indeed be more significant at higher current densities. When the current rate was kept below 1 mA/cm^{2}sec polarization rarely developed, even when current densities were as high as 10 A/cm^2.

It is also possible that impurities in the sodium would have assisted in the deterioration of the surfaces of these electrolytes. The surfaces of the electrolytes were therefore examined by means of energy dispersive X-ray spectroscopy in the scanning electron microscope. The only impurity which showed up consistently on the sodium entrance surface was potassium. Figure 24 shows an SEM micrograph of the sodium entrance surface of cell 90613 after 20 A hrs/cm^2 of unidirectional charge transfer, with a potassium peak identified, Figure 25. Potassium-beta alumina has a substantially higher resistivity than its sodium counterpart and its C_0 lattice parameter is also significantly
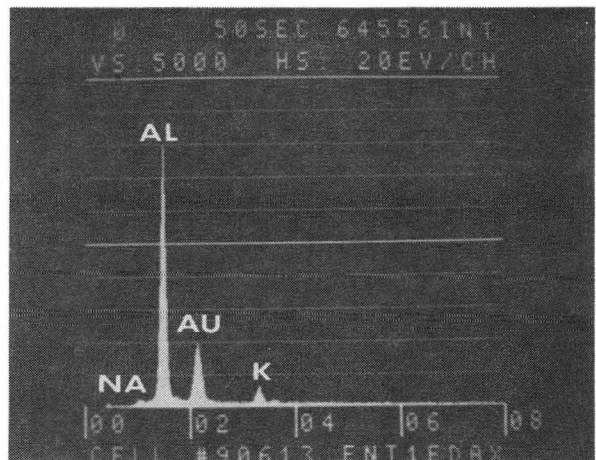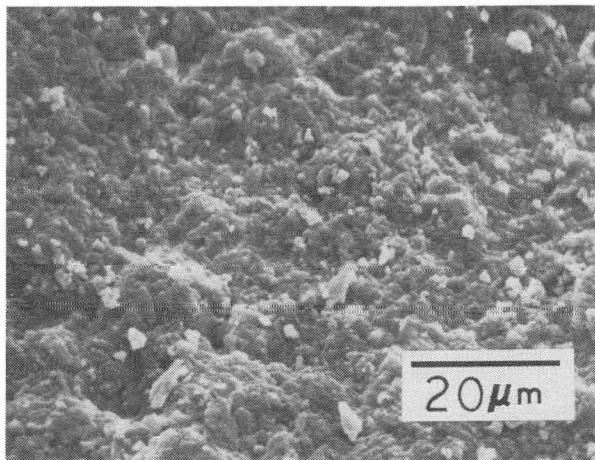
Figure 24. (a) Scanning electron microscope micrograph of sodium entrance surface after 20 Ahr/cm^2 of unidirectional charge transfer. (b) X-ray dispersive analysis of the surface shown above, identifies potassium
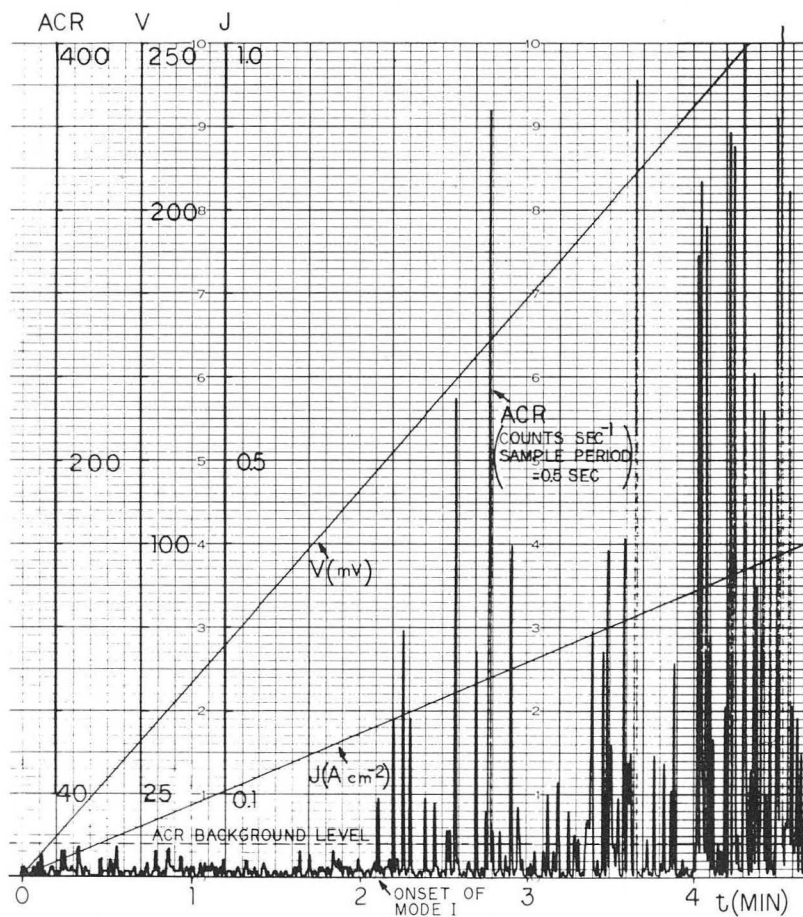
Figure 25. Current Density (J) and Voltage Data (mV) Superimposed on Acoustic Count Rate (ACR) for Sodium/Sodium Test Cell 00626, V in Millivolt, J in A/c^2, ACR in Counts/sec.

different. The assimilation of potassium into the surface of the electrolyte should therefore contribute to the polarization and degradation of the cell. This has already been shown by Fally et al. (6). One factor to be considered in the buildup of impurities at the electrode/electrolyte interface is that only sodium can enter readily into the electrolyte, so that a high concentration of impurities as a result of cell cycling could build up at the interface even if the impurities are only present at low levels in the electrodes. A sufficient build-up of impurities, such as potassium, at the electrolyte/electrode interface could produce stresses after some exchange of ions, which would increase susceptibility of the surface to cracking.

Polarization and short circuit phenomena can be readily followed by monitoring cell currents and voltages versus time. Interpretation of the current-voltage time data is, however, not always straightforward, particularly when unstable interface polarizations interfere with the formation of partial short circuits.

Acoustic emissions monitoring is therefore a more reliable means of finding the current densities at which the Mode I degradation is initiated. Figure 25 shows typical current and voltage versus time data superimposed on acoustic emission rate data. The onset of increased acoustic activity is evident.

As for the critical current density data collected below 100°C, the present data, all collected at 350°C, have been represented in Weibull statistical plots of $\ln \ln[1/(1 - P_f)]$ vs j_{crit}. Sofar only the "10" µm grain structure and the "300" µm grain structures have been tested. A clear difference can be observed, as follows from Figure 26. In contrast to the experiments below 100°C, the 350°C experiments indicate a clear dependence on the microstructure of the material. This time, the average threshold current densities correlate well with the grain size: an increased grain size or increase in the fraction of very large grains causes a drop in the average current density at which the Mode I degradation is initiated. The different correlations between microstructure and current density threshold appears to suggest that the testing below room temperature activates a different part of the spectrum of surface flaws. This draws into question the relevance of current density threshold determinations or even the concept of proof testing below the melting point of sodium. Certainly, proof testing on hot cells, while of more significance, would call for a rather complicated test-use transfer.
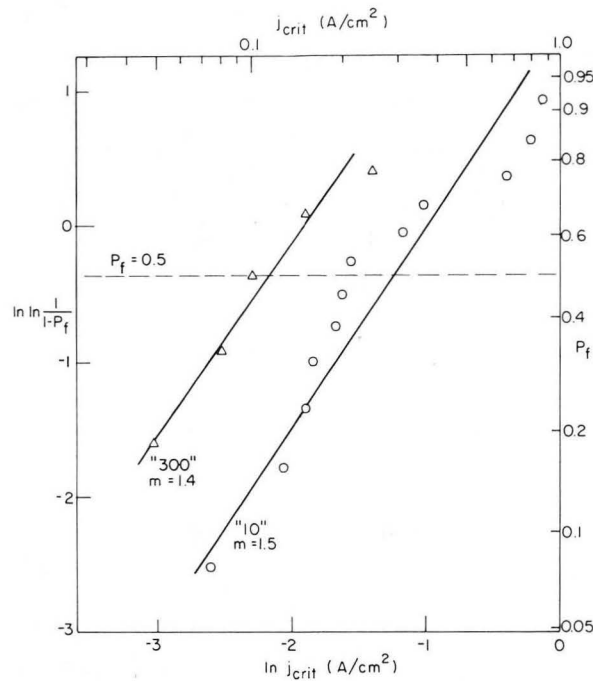
Figure 26. Weibull Plot of Critical
Current Density in a Sodium/Sodium Cell
at the 350°C for the Two Indicated
Microstructures

The average current densities for initiation of Mode I failure are significantly
lower than those reported by other investigators (7). The difference in
criterion used is possibly the basis for the discrepancy. We tend to believe,
however, that the acoustic emission detection is more sensitive than a strength
test after electrolysis (7).

Microstructural Aspects of Mode I Degradation Initiation

There are several factors which can contribute to introducing a statistical
spread in the critical current density or voltage that is necessary to propagate
a small pre-existing flaw. These factors are associated with the intrinsically
heterogeneous microstructure of the sodium beta alumina polycrystalline
electrolytes. One such factor is the local electrode current density as
discussed in a previous section. Another factor is the local geometry of a
small flaw that serves as a nucleus for failure by Mode I. The Mode I failure
initiation presupposes the existence of small surface flaws typically between 1

to 20 micrometers long, with a crack opening that is determined by the current density. Once such a flaw is filled with sodium by the electrolysis process, current focussing occurs and the Mode I mechanism can operate.

Beta aluminas are extremely anisotropic conductors, and frequently blocking grain boundaries can be found. The local microstructure will therefore strongly alter the current flow into the cracks, especially when these cracks are on the order of the grain size. Simple geometrical considerations show that the cracks are most effectively current fed when they are oriented perpendicular to the conduction planes, as shown in Figure 27A. However, beta alumina cleaves most readily parallel to the conduction planes. If the initiation flaw were approximately parallel to the conduction planes, the local anisotropy would not permit it to be effectively current fed on its faces. Instead, feeding of the crack through electrolysis would have to depend on local deviations of the crack plane from the cleavage plane. The next most favorable geometry is the one shown in Figure 27B and involves a blocking grain boundary that is faceted along conduction planes. The total ionic current gathered by such a crack is 1/2 that of a crack oriented perpendicular to the conduction planes. Additionally, the microstructure of beta alumina will introduce heterogeneous electrode or near electrode current densities, so that statistical fluctuations may be expected in the actual current density threshold at which degradation will be initiated. It
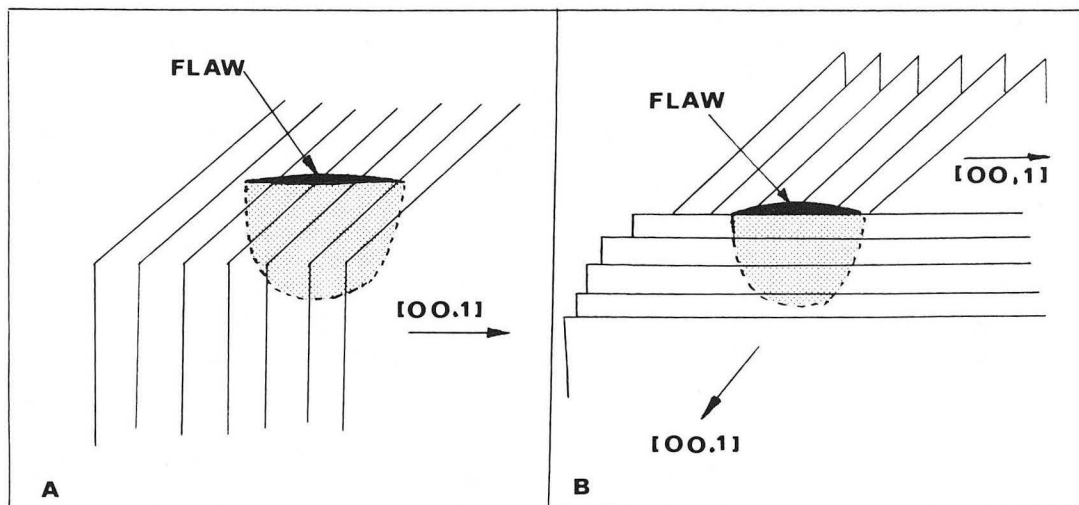
Figure 27. Flaw Geometries for Initiation of Mode I; (a) Most Favorable Geometry, (b) Next Most Favorable Geometry.

is, therefore to be expected that current densities at which flaws first start to propagate can vary easily by as much as a factor of 5. The problem of determining the critical current density for Mode I flaw propagation in an actual polycrystalline electrolyte is therefore an extreme value statistical problem, as was implied in the test results on failure initiation.

To verify the influence of the electrolyte microstructure on the location of the Mode I initiation sites, three Na/Na cells were made of "300" μm Na-β" alumina electrolytes with a polished surface section. These cells were cycled once so that the polished sections were only an Na exit or entrance surface. The results are shown in Figures 28-30. After removal from testing the electrolytes were silver stained. Clearly, there is a significantly greater degree of grain boundary decoration on the sodium exit surfaces compared to the entrance surfaces. It is therefore concluded that grain boundaries are the most active sites in the early stages of Mode I degradation, in agreement with the simple geometrical considerations given above. The less extensive decoration of the
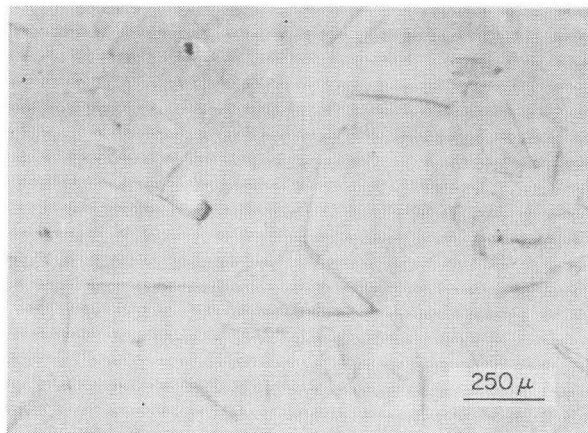
Figure 28. Decoration of Polished Sodium Exit Surface of Large Grained Electrolyte in Sodium/Sodium Cell
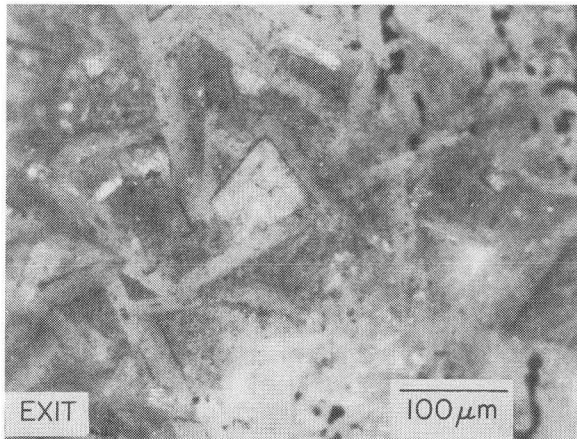
Figure 29. Decoration of sodium exit surface of sodium/sodium cell. Note extensive darkening of the grain boundaries of the large grains
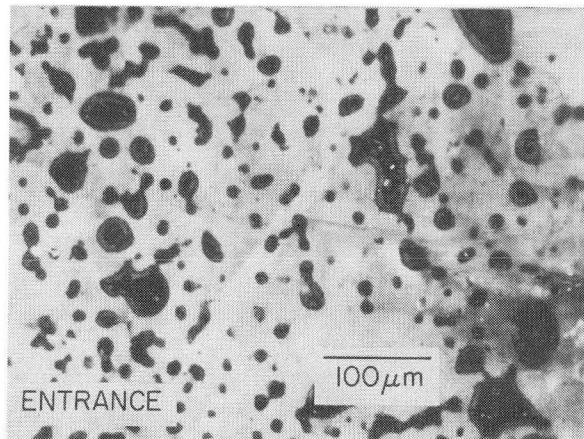
Figure 30. Decoration of sodium entrance side of a sodium/sodium cell with the same history as those of Figures 28 and 29. The dark patches are sealing glass that accidentally contaminated the polished surface during cell fabrication. Still, there is much less evidence of grain boundary decoration for this sodium entrance surface.

sodium entrance surface is consistent with the postulate that under normal circumstances there is no mechanism expected to produce degradation there. However, under conditions of severe polarization, we found evidence of degradation at the sodium entrance surface, as discussed before.

MODE I FAILURE PROPAGATION

To clarify the nature of the Mode I failure some experiments were performed that examined the propagation stage of this type of degradation. Experiments and observations are reported here on single and polycrystals of Na-beta alumina at room temperature with a variety of electrode types, and on polycrystalline Na-beta" alumina at 300°C tested in the Na/Na cells.

Single Crystals of Na-Beta Alumina at Room Temperature

Small single crystals 0.1 centimeter x 1 centimeter were cleaved from a larger single crystal. The cleavage plane was the conduction plane. Sodium metal formation was initiated with either blocking or non blocking electrodes as shown
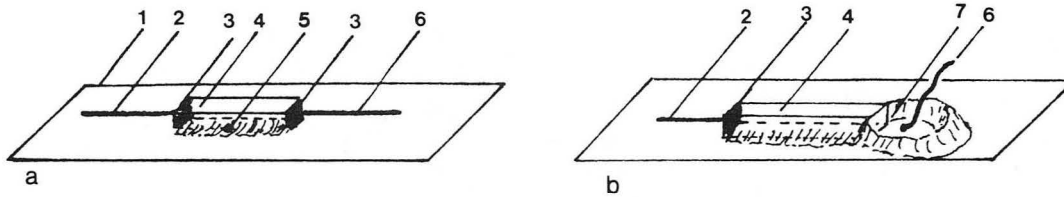
Figure 31. Electrode arrangements for room temperature DC breakdown. Configuration A, two gold blocking electrodes; Configuration B, negative electrode blocking, positive electrode non-blocking. 1. Glass slide, 2. Negative electrode lead, 3. Gold blocking electrode, 4. Electrolyte, 5. Mounting glue, 6. Positive electrode lead; 7. Positive electrode reservoir for alcohol-sodium iodide solution.

in Figure 31. With the two blocking electrodes, configuration A, Mode I breakdown was observed to occur at applied voltages of about 700 volts. The breakdown was readily visible as a small reflecting sodium-filled crack emanating from the negative electrode.

In configuration B, with a non-blocking supply electrode, Mode I breakdown occurred at around 40 volts per centimeter. The geometry of the metal formation was very similar in both cases. In case A, an anodically depletive situation, the breakdown did not progress after the initial rapid breakdown event unless the voltage was raised further. In case B, the anodic supply situation, the breakdown progressed rapidly at constant voltage until the metal reached the positive supply electrode. At the same time, metallic sodium slowly seeped out of the crystal sides, where the conduction planes intersected the surfaces, reacting with the ambient air and moisture.

The geometry of the breakdown is clearly shown in Figure 32. The metal that is formed is highly reflective, permitting direct interferometric study of the cleavage plane. Also, evaporation on some gold on one of the surfaces of the single crystal permitted determining the approximate size of the metal-filled crack opening, assuming the crack opening displacement was symmetrical with respect to the surface of the crystal (the cleavage plane). The results of these examinations are shown in Figures 33A and 33B for breakdown produced with two blocking electrodes (configuration A in Figure 31).
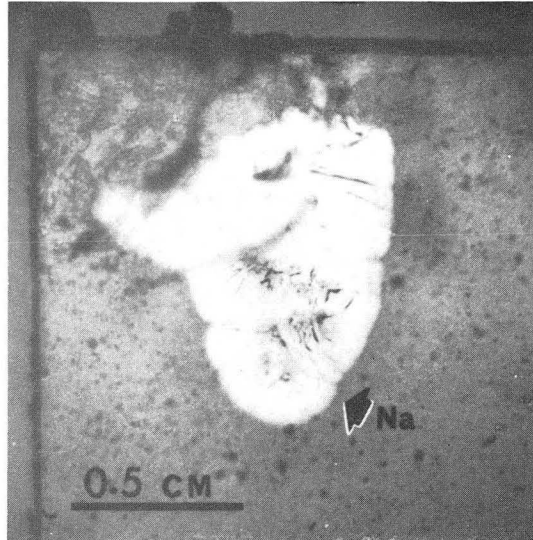
Figure 32. Sodium metal formed at netative
electrode in DC breakdown of a sodium–beta
alumina single crystal. The sodium metal at
the top of the picture has reacted with
atmospheric oxygen and moisture
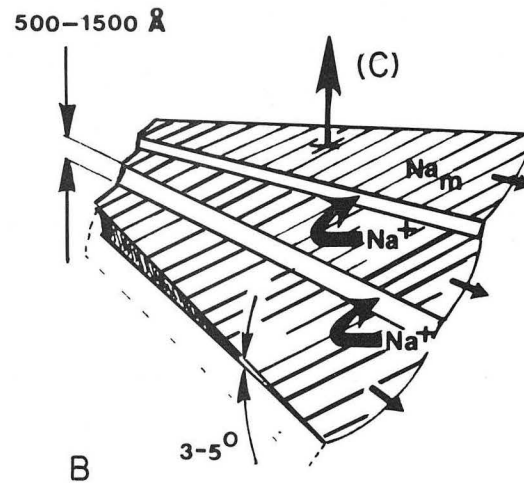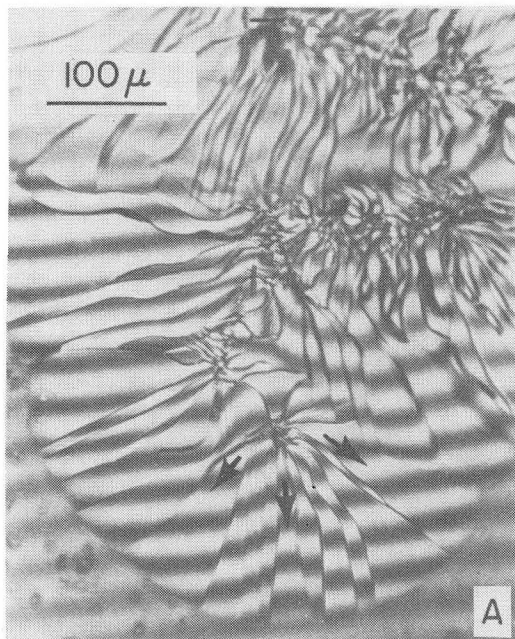
Figure 33. Geometry of Sodium Filled Crack (a) Interferometry
Observation, (b) Geometry Derived from the Interferometry

It is clear that depleting of a single conduction plane cannot provide sufficient sodium to fill such a large crack. Therefore, the crack must have been fed from the steps, or river marks that intersect the many conduction planes. Since the crack propagation mode and morphology was identical in the configuration where the positive electrode is supplying sodium ions the crack steps play an important role as sites where sodium is fed into the crack in all cases. The observations indicate that for Mode I propagation, one cannot simply assume that the crack is only tip fed. This introduces a serious difficulty in the modeling of sodium-filled crack propagation due to current passage in beta alumina, since the critical stress intensity factor depends strongly on the distribution of the current on the crack faces.

Polycrystals of Na-Beta Alumina at Room Temperature

Only the non-blocking supply electrode configuration, Figure 31B was used. For most electrolytes breakdown occurred around 40 volts. The degradation manifested itself as a somewhat diffuse blackening propagating through the sample. An attempt was made to determine the rate of propagation of the blackening. It was found that at constant macroscopic current density, the rate of propagation of the degradation was approximately constant. Definitely no increased rate with increased degradation length was observed under these conditions. An interesting feature of these breakdown experiments is that the electrolytes start showing many surface cracks that accompany the sodium metal filled crack propagation. The metal seeps out of these cracks and reacts with the ambient. Figures 34A and 34B compare the polycrystalline surfaces in the breakdown region near the negative electrode and in the unaffected region near the positive electrode. The difference is obvious. This phenomenon points to the highly branched nature of the metal filled crack propagation under these conditions.

Both the experiments on the single crystals and on the polycrystals demonstrate the difficulty of the available models to deal adequately with the propagation stage of the Mode I degradation. Branching of the degradation crack network should be considered, and only those models can be accepted that lead to a constant propagation rate. On the basis of this last point, the model for Mode I failure first proposed by Armstrong et al. (8) needed to be modified. Such modifications have been recently proposed by Virkar et al. (9).
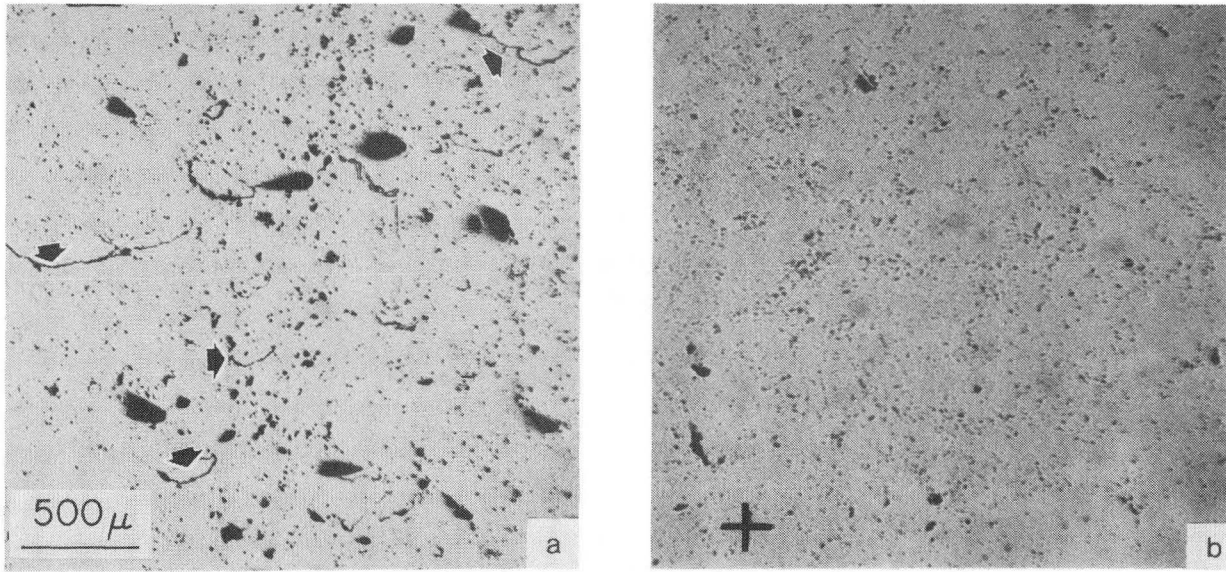
Figure 34. Surface cracks (arrowed) developing in association with the breakdown propagation. (a) Cracked region near negative electrode; (b) Unaffected region near the positive electrode

Na-Beta" Alumina Polycrystals at 300°C

One of the consistent features noted in cells cycled to failure was the formation of cracks of the type shown in Figure 35. These cracks were roughly parallel to the electrolyte surface, i.e., perpendicular to the current flow.
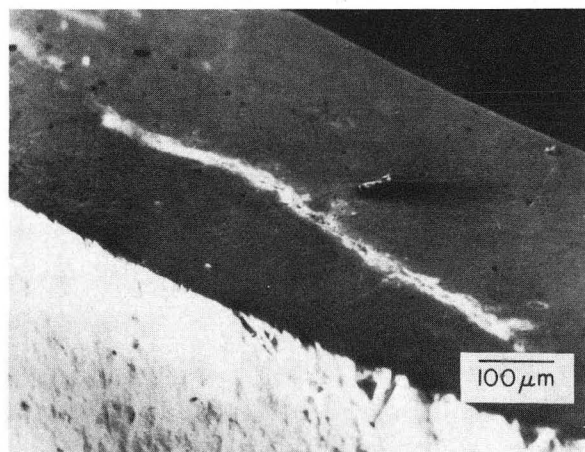
Figure 35. Circumferential Crack Produced in Electrolytes Tested in Sodium/Sodium Cells

This phenomenon is due to a basic instability in the crack propagation: a sodium filled crack is more effectively current fed when it is oriented perpendicular, rather than parallel to the current flow. Such cracks can lead to spalling of the electrolyte at the sodium/electrolyte interface. Most frequently these cracks propagate inside the electrolyte wall, around the tube. When tubes containing cracks of this type are removed from the sodium/sodium cells, it appears as if they contain large dark patches in their interior.

Often, the electrolytes exhibit various micromorphological indications of breakdown after testing to failure. Figure 36 shows this for cell 90521. The electrolyte in this cell had the "300" μm grain structure. It was subjected to 10.2 A hr/cm^2 of charge transfer, and to a maximum current density of 11 A/cm^2 before catastrophic failure occurred. The crack network that had formed had branched heavily, as is clearly visible through the translucent larger grains. This crack branching must obviously have occurred before the ultimate failure of the cell. Figure 37 is a cross-section of cell 90530 showing extensive diffuse darkening and many cracks which are for the most part perpendicular to the direction of current flow. This cell was made up with the "10" micrometers material and was subjected to 254.7 A hrs/cm^2 of charge transfer.
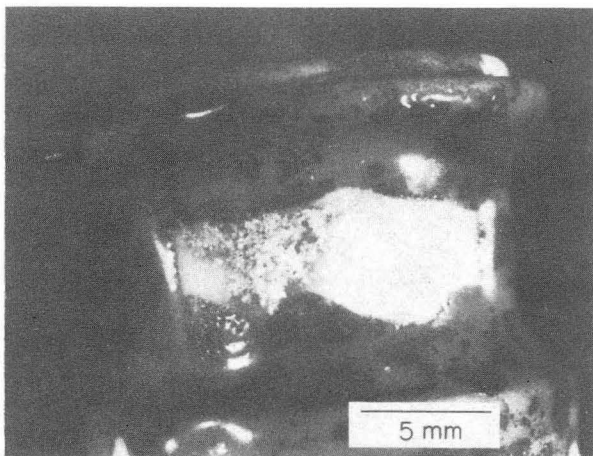
Figure 36. Sodium entrance surface of cell 90521 after breakdown in sodium/sodium cell test. The electrolyte was the "300" μm grain structure, subjected to a total of 10.2 A hr/cm^2 and to a maximum current density of 11 A/cm^2 before catastrophic failure occurred.
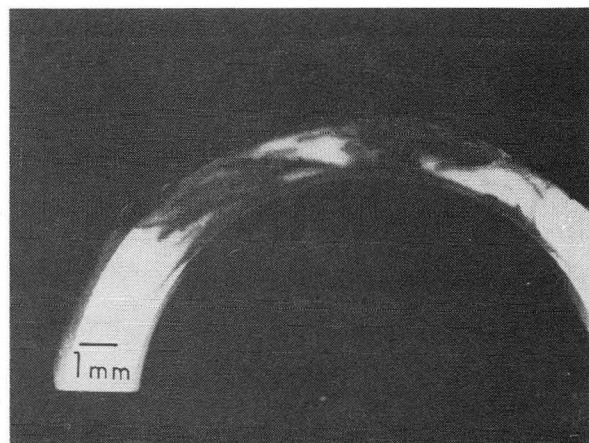
Figure 37. Cross section of cell 90530 showing extensive diffuse darkening and many cracks. This cell was made up of the "10" micrometer material and had been subjected to about 255 A hr/cm^2 of charge transfer

Silver decoration of the sodium/sodium cells revealed the same interfacial darkening observed in electrolytes from tested beta batteries, but now proceeding inwards from both Na/electrolyte interfaces. Sections of cells 90901 are shown in Figures 38a and 38b. This cell had been subjected to 65 A hrs/cm^2 of charge transfer and a maximum current density of 6 A/cm^2 when removed from testing, but not yet failed catastrophically. Apparently, significant cracking may be tolerated before a complete short circuit is established. The predominant orientation of the cracks was again perpendicular to the direction of current flow. Silver decoration was used here to highlight the darkened layers and cracks near the electrolyte surfaces. A large crack is seen originating at the sodium exit surface. The enlarged detail, Figure 38b, is a region on the sodium exit surface which had sealing glass adhering to it. A crack had initiated at the edge, but was quickly deflected. Although branched, the crack bundle is mainly perpendicular to the direction of current flow.

These observations again indicate the complexity of the Mode I breakdown propagation. The way the sodium filled cracks propagate in the Na/Na test cells appears to be similar to the propagation geometry of cracks in beta battery electrolytes. Spalling, and circumferential cracks propagating internally
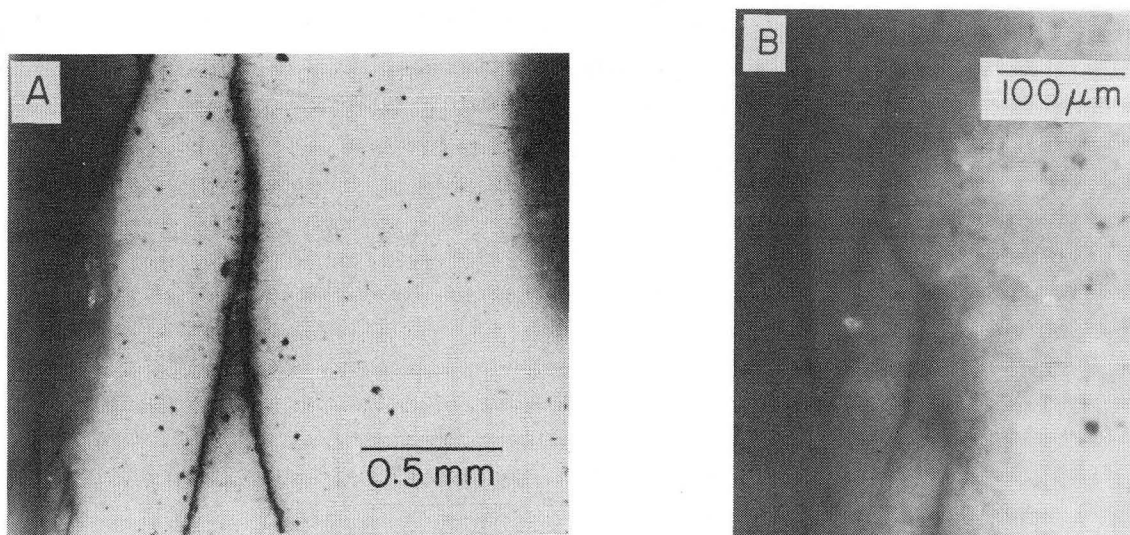
Figure 38. A and B sections of 90901. This cell had been subjected to 65 A hr/cm^2 and a maximum current density of 6 A/cm^2, but had not yet failed catastrophically in the sodium/sodium cell test

parallel to the electrolyte surface have been reported by British Rail and have been found by us in used General Electric beta battery electrolytes (see later in this section).

CHEMICAL COLORATION

When sodium-beta or beta" alumina solid electrolytes are in prolonged contact with molten sodium metal, they discolor noticeably. The grey-brown discoloration can be attributed to the chemical action of the molten sodium on the electrolyte, since the darkening occurs without current passage. Coloration slowly develops as a layer from the sodium electrolyte interface. Since slow degradation of the electrolyte could occur in sodium/sulfur cells as a result of prolonged ionic current passage it is necessary to clarify the nature of the chemical darkening to understand which role it could possibly play. A series of experiments on sodium-beta alumina single crystals and on sodium-beta" polycrystals of different grain sizes was conducted to elucidate the nature of the chemical coloration.

Single crystals of sodium-beta alumina, packed in coarse sodium-beta alumina powder, were annealed in air at 1600°, for two hours. This treatment was necessary to eliminate all absorbed water and to partially heal the basal plane cleavage cracks that tend to develop in large sodium-beta alumina single crystals. The crystals were cut in kerosene to a size of about 3 x 5 x 8 mm. The polycrystalline sodium-beta" alumina with the "10," "150" and "300" μm grain structures were also used. The samples were dried in air at 800°C for two hours and immediately immersed in molten sodium for up to 16 days. Temperatures were controlled to within ±1°C between 200 and 400°C. The experiments were performed under argon, in a glove box. Some oxidation of sodium appeared to be unavoidable and the molten metal should therefore be considered to be saturated with oxygen. At 350°C, this puts the oxygen fugacity at about 10^{-55} atm in the molten sodium. After immersion, the samples were sectioned. A discoloration was present in all samples. For one section of each specimen, the discoloration could be strongly enhanced by silver exchange of the sodium in molten $AgNO_3$, at 300°C, for 20 min. The coloration profiles of the polycrystalline specimens was then traced with a microdensitometer from micrographs of the silver stained coloration layers.

The obtained profiles were all normalized with respect to the photographic

density at the Na/electrolyte interface. The rate of propagation of the coloration was determined from the distances, x, in the profiles where erf(x/g Dt) = 0.5. For simple diffusion control, this criteria would give D = x^2/0.92t, provided the densitometer trace corresponded quantitatively to the concentration profile. It was not possible to verify the exact relationship between optical density and concentration of the coloration defect; however, a qualitative correspondence should exist permitting determining coloration defect diffusion rates that are fairly reliable.

The coloration of the single crystals appeared to occur in a more discrete layer and the coloration propagation rate could be measured directly from the layer thickness after staining one part of each specimen. The other part of these single crystal specimen sections was reheated in air at temperatures between 200 and 600°C. This led to a bleaching that proceeded from the surface, again as a discrete layer. The thickness of the bleached layer could be measured optically after silver staining.

To verify the effect of the adsorbed surface water on the bleaching rate, some single crystalline samples were partly bleached after exposure to air containing 50 percent H_2O at 20°C, cooled, reexposed to the moist air and bleached again.

To investigate the role of oxygen in the bleaching phenomenon, colored samples were heated in an evacuated quartz ampule. The ampule also contained a vanadium foil. The vanadium was heated separately to about 700°C to remove all oxygen involved. This provided an atmosphere where the oxygen partial pressure was below about 10^{-38} atm.

Polycrystals of sodium-beta" alumina and of silver exchanged beta" alumina were partly masked and irradiated for 1 min with an intense UV beam. The cutoff wavelength corresponded to a photon energy of about 10 eV. These specimens were then examined for discoloration. This experiment could give an indication of the role of free electrons and holes in the coloration process.

Detailed transmission electron microscope observations of chemically discolored, polycrystalline sodium-beta" aluminas failed to reveal any features that could be attributed to the discoloration. This strongly suggests that the chemical coloration involved point defects rather than formation of second phases. The

results of the experiments have therefore been interpreted in terms of point defects.

From the time scale that was involved in the formation of the coloration zones, the published evidence of Na^+ diffusion through the spinel blocks (10), the expected diffusivity of the aluminum ions and the approximate electron transport rates (11), it was concluded that the chemical coloration could involve only transport of electrons or holes, of sodium, or of oxygen either by oxygen vacancies or by hydronium ions.

Single Crystal Experiments.   The chemical coloration of the single crystals appeared to proceed more or less isotropically. This is shown in Figure 39. When colored crystals were heated in air, the bleaching surprisingly occurred only in the direction of the conduction planes, as shown in Figure 40. Alternating current conductivity measurements indicated that the ionic conductivity was little affected by the coloration and by the bleaching process. Colored single crystals heated in the evacuated quartz ampules for times up to 24 hrs at 400°C did not show any signs of bleaching from the exposed surface as is evident from Figure 41.
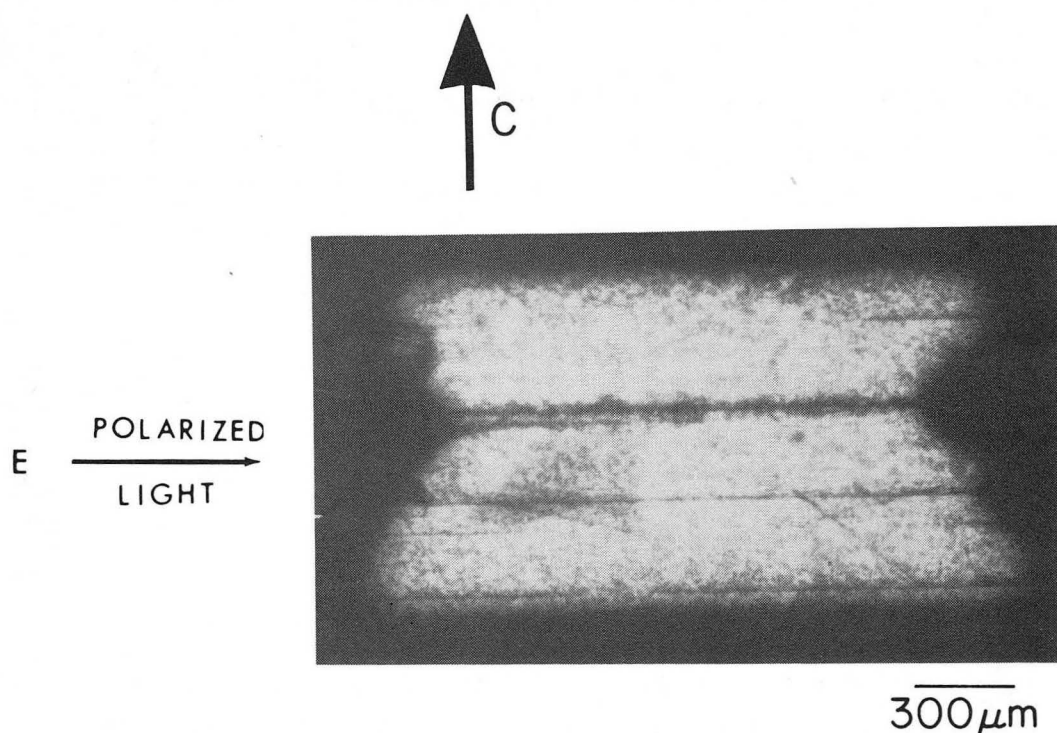
Figure 39. Approximately isotropic chemical coloration of single crystal of sodium—beta alumina immersed in sodium at 350°C
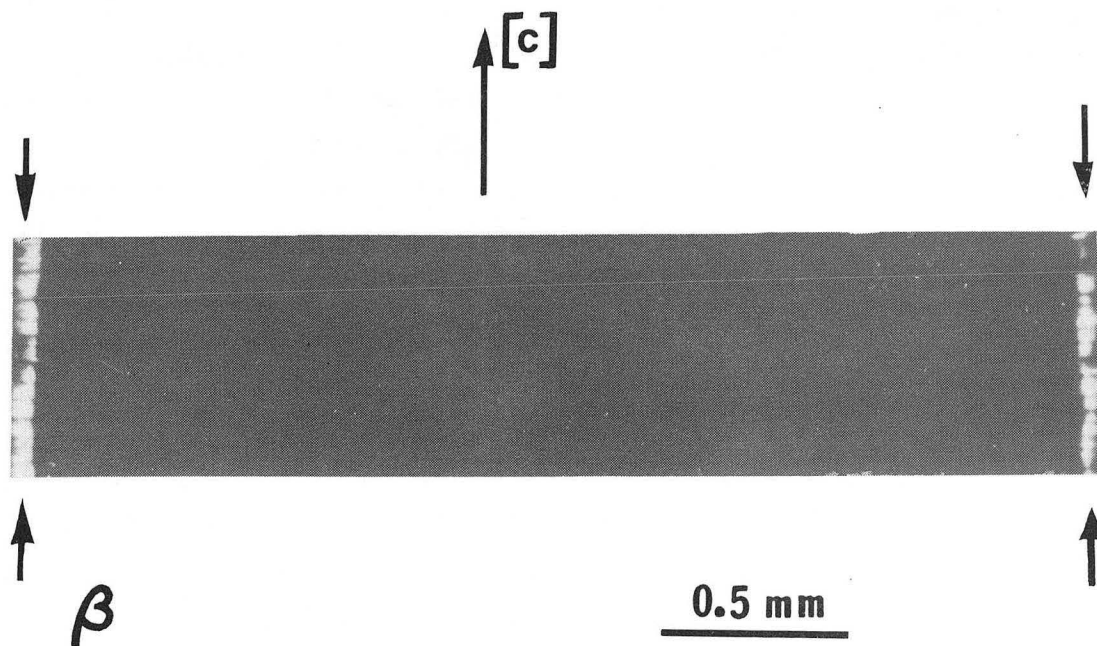
Figure 40. Anisotropic bleaching of chemically colored single crystal heated in air for 16 hrs at 300°C
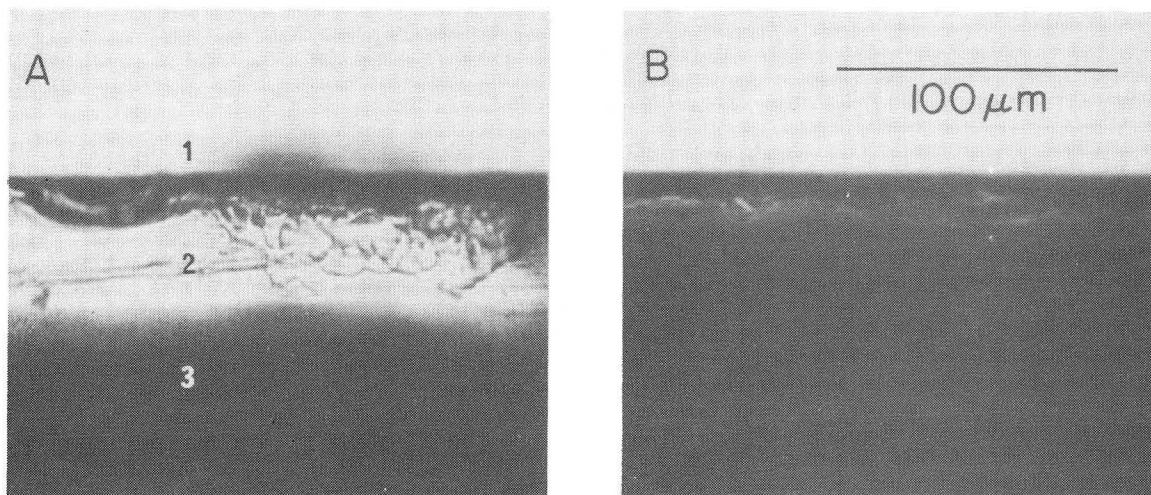
Figure 41. Comparison of chemically colored single crystals heated in air (a) and heated in vacuum (b). Bleaching did not occur for the chemically colored crystal heated in high vacuum. Areas designated are: 1. edge of crystal, 2. Bleached layer, 3. Unbleached crystal.

These results establish that the coloration must involve removal of oxygen from the sodium-beta aluminas, while the bleaching involves reoxidation. The coloration appears at a broad optical absorption indicating that electrons are involved as well. Additionally, it was found by Weber ($\underline{12}$) that chemical coloration at high temperatures appears to lead to a measurable increase in

electronic conductivity. It is therefore concluded that the coloration of sodium-beta aluminas by molten sodium metal is a reduction of the electrolyte in which the oxygen vacancies that are introduced are charge compensated by electrons. The detailed nature of the defect causing the light absorption is not known at present. Possibly, a local sodium ion redistribution may be associated with it which together with the oxygen vacancy and a weakly bound electron would give the rather broad optical absorption.

The remarkable asymmetry in the coloration/bleaching reaction needs to be explained. It is believed that the answer may lie in differences in the dependence on oxygen partial pressure of the oxygen vacancy diffusion rate in the spinel blocks and the conduction planes of the crystals. To demonstrate that oxygen vacancy injection could occur through the spinel blocks, a single crystal was covered with sealing glass except for an exposed basal plane section, as shown in Figure 42a. The darkening pattern after contact with molten sodium, Figure 42b, clearly indicates that the coloration proceeded through the spinel blocks. The oxygen vacancy diffusion rate through the spinel blocks would have to depend much more strongly on the oxygen partial pressure than that of the conduction planes: in oxidizing conditions, the oxygen vacancy concentration of the spinel blocks would be so low that oxygen ion transport is effectively suppressed while the more open structure of the conduction planes would not be so strongly affected. The fact that coloration is observed to
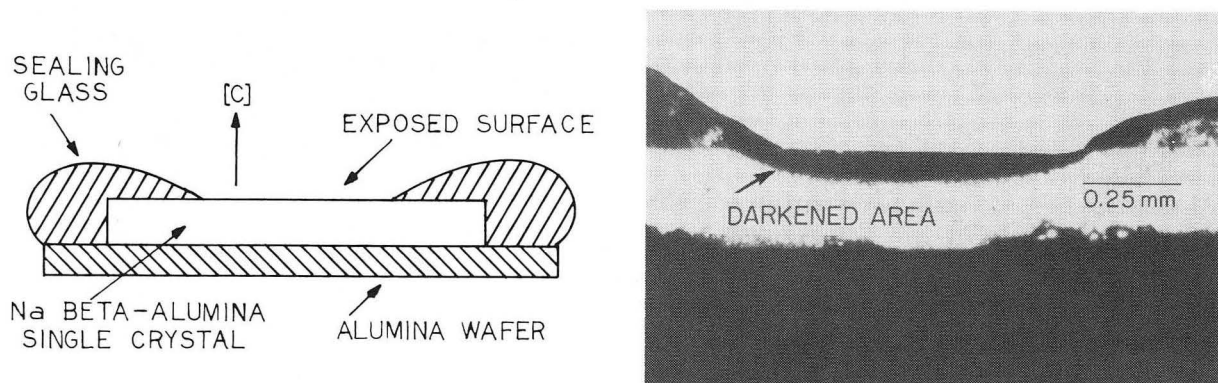
Figure 42. (a) Configuration for Unidirectional Exposure of Single Crystal (b) Darkening Pattern after Contact of Molten Sodium Indicates that the Coloration preceeded through the Spinel Blocks

proceed in a layer-like fashion supports this type of explanation. Indeed, a strong oxygen partial pressure dependence of the oxygen vacancy diffusion rate would lead to a fairly abrupt vacancy concentration profile change. Thus, in oxidizing atmospheres, oxygen exchange would effectively occur through the conduction planes only. This explanation additionally requires that bleaching would occur more slowly than coloration. This was indeed the case, as follows from a comparison of coloration and bleaching rates in Figure 43. Some further elucidation of the nature of the coloration defect followed from the U.V. irradiation of Na- and Ag-beta" aluminas. The U.V. photons produced darkening in the silver-beta" aluminas, as is evident in Figure 44. The photon energies ranged up to 10 eV so that electron-hole pairs could be created directly. The darkening produced by U.V. irradiation should then be analogous to the photographic imprinting effect where silver ions capture the electrons to form metallic silver, leaving an electron hole. Photodarkening could not be produced in the Na-beta" or beta alumina. This indicated that the sodium ions do not readily trap electrons, further corroborating that coloration cannot be attributed simply to a sodium-electron pair.

Effect of Adsorbed Water or H_3O^+ Substitution. No effects, either in appearance or kinetics, were detected on either the coloration or the bleaching
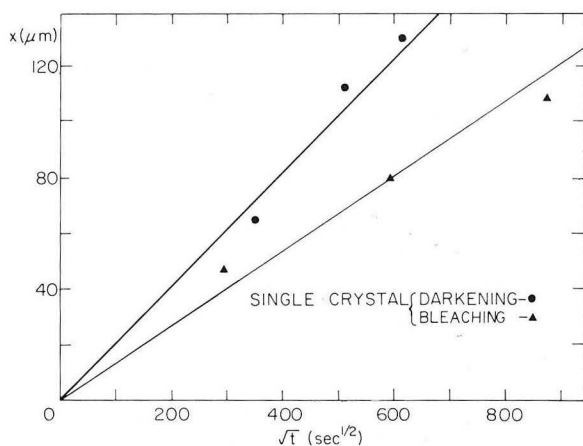
Figure 43. Comparison of Coloration and Bleaching Rates
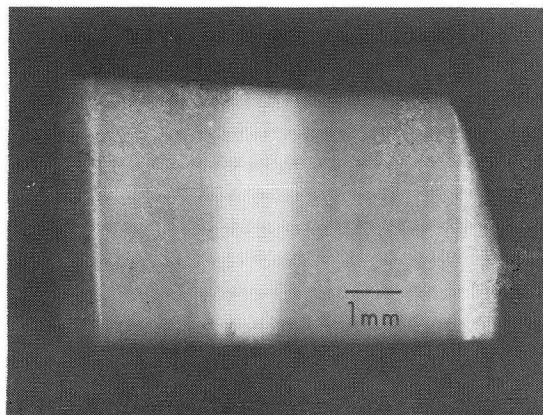
Figure 44. Partial coloration of a silver-beta alumina produced by high energy UV irradiation. This shows that free electrons created by UV irradiation can lead to silver precipitation. This does not happen in sodium-beta or -beta" alumina

of those crystals that had experienced repeated water absorbtion and bleaching, or that contained some H_3O^+. This indicates that the coloration cannot be attributed to effects of water.

Polycrystal Experiments.   The results of chemical coloration experiments at 350°C on the polycrystalline electrolytes are shown in Figure 45. The rate of coloration propagation is substantially faster in the small grain size electrolyte. This establishes that the grain boundaries act as rapid transport paths for coloration producing defects.

The data permit evaluation of the approximate bulk and grain boundary transport rates by use of the Hart analysis (13). This analysis can be applied if the mean penetration distance is much larger than the average grain size. This condition was satisfied in our experiments. In that case, the apparent diffusion coefficient, D^{eff}, can be related to the lattice diffusion coefficient, D_L, and to the grain boundary diffusion coefficient, D_B.

$$D^{eff} = D_L + B\delta D_B/s$$

where B is a geometric parameter about equal to 1, δ is the grain boundary thickness which is on the order of 10Å, and s is the average grain size. The data are summarized in Table II.
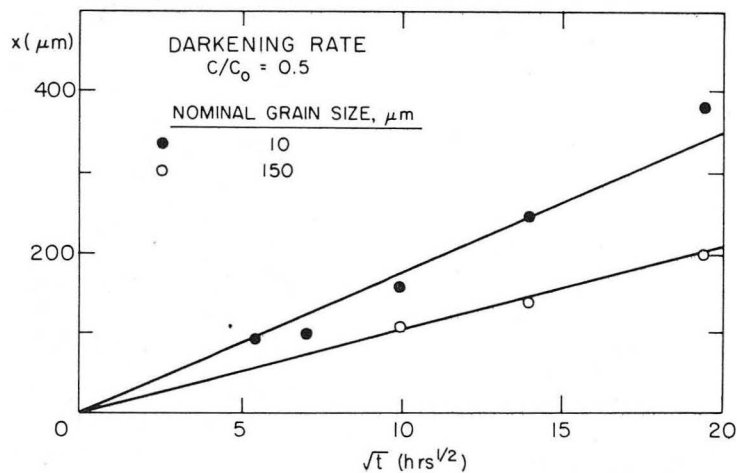
Figure 45. Comparison of chemical coloration rates at 350° on "10" and "150" micrometer electrolyte. The rate of coloration propagation is substantially faster in the small grain size electrolyte

Table II

COLORATION KINETICS AT 350°C

Material	D^{eff} (cm^2/sec)	Average grain size (μm)
"10" μm β"	9.8×10^{-10}	1.1
"150" μm β"	3.0×10^{-10}	5.4
Single crystal β	4.5×10^{-10}	

This leads to the following results:

for β": $D_L = 1.0 \times 10^{-10}$ cm^2/sec

$D_B = 9.8 \times 10^{-7}$ cm^2/sec

for β: $D_L = 4.5 \times 10^{-10}$ cm^2/sec

It can then be observed that the ratio of grain boundary to bulk diffusion rates, D_B/D_L, for the β" polycrystals examined here is about 10^4. Clearly, grain boundary diffusion dominates the kinetics of coloration in polycrystalline electrolytes. It should thus be expected that the partial electronic conductivity associated with the coloration develops first along the electrolyte grain boundaries. A rough estimate of the time needed to complete homogenization of a 2 mm wall thickness β" electrolyte, in contact with Na at 350°C would be 0.5 years. It should be emphasized, though, that the sulfur electrode side of the electrolyte is not at the same oxygen chemical potential as the sodium electrode side. The oxygen fugacity in the sulfur electrode is not known, but is likely to be substantially higher than that in the sodium electrode. As a consequence, it should be expected that in beta batteries an electronic transport number gradient should persist indefinitely.

FAILURE ANALYSIS OF ELECTROLYTES FROM BETA BATTERIES

Sodium Side

The electrolytes used were obtained from the General Electric Research and Development Center. They were beta-alumina electrolytes with a composition of

9.6 wt % Na_2O; 0.25 wt % Li_2O; balance Al_2O_3. The starting material was a commercial sodium beta-alumina powder containing approximately 7.5 weight percent Na_2O, with about 0.15 weight percent SiO_2 as the major impurity (Alcoa-XB-2 "Superground," Aluminum Company of America, Pittsburgh, Pennsylvania). The electrolytes had been cycled in sodium/sulfur cells at current densities of approximately 100 mA cm^{-2}. The cells operated at around 300°C and were cycled into the two-phase region of the sodium polysulfide electrode. After cycling, the cells were cleaned with methanol and stored prior to examination in our laboratory. During storage, the cells were exposed to atmosphere for a period of about 1 week.

The surfaces of as-received electrolytes and of sectioned and polished electrolytes were examined by optical microscopy. It was necessary to use silver staining to reveal the flaws. The staining was carried out in a one molar aqueous solution of silver nitrate at a temperature of about 80°C for between 0.3 and 1.0 hrs. Comparisons of the electrolytes show that this staining procedure did not introduce any additional flaws that could be detected by optical microscopy. The stained electrolytes were examined using polarized light to reduce the surface scattering. Additional observations on unstained electrolytes were performed by scanning electron microscopy, high-voltage transmission electron microscopy and analytical transmission electron microscopy.

Chemical Coloration. Chemical coloration was also present in the electrolytes examined and discussed here. The layer grows, however, far more rapidly than the Mode II degradation layer described below. At 300°C it has proceeded about 0.5 mm into the electrolyte after immersion in molten sodium for approximately 10 days. This puts D^{eff} at approximately 7 x 10^{-10} cm^2/sec, in good agreement with our laboratory tests on β" electrolytes. Transmission electron microscopy of the discolored regions again failed to reveal any imperfections that could be attributed to the chemical darkening.

Mode II Degradation. Stained sodium/electrolyte interfaces of four cells are compared in Figure 46 after a total charge transfer (charge + discharge) ranging from 23 to 703 Ahcm^{-2}. A progressive though uneven darkening is observed. These surfaces were more closely examined by optical microscopy, Figure 47, but did not reveal any resolvable features of significance. An important
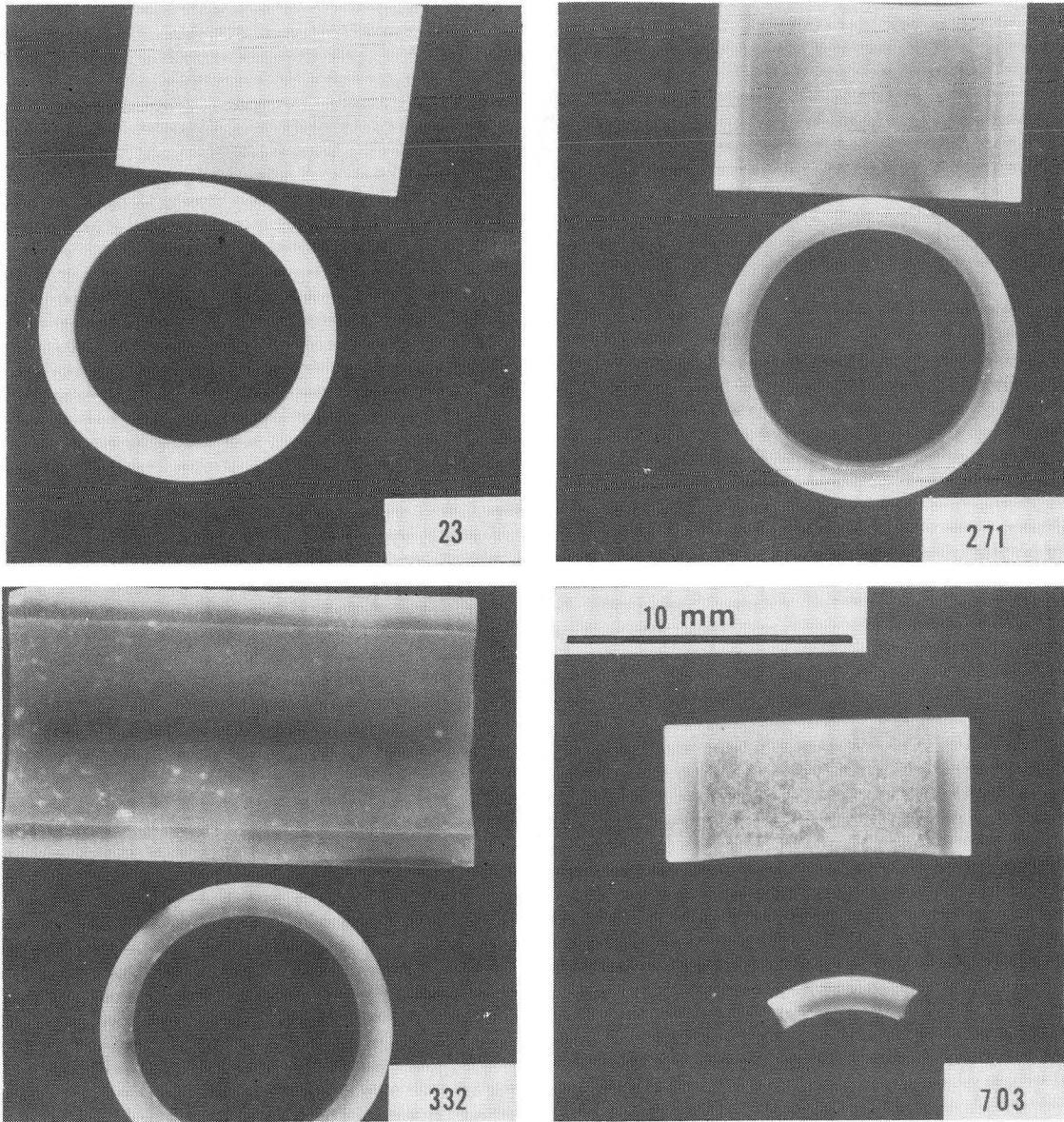
Figure 46. Comparison of silver stained sodium/electrolyte interfaces of four electrolytes used in beta batteries. The total charge transfer (charge + discharge) ranging from 23 to 703 A hr/cm^2 has been indicated
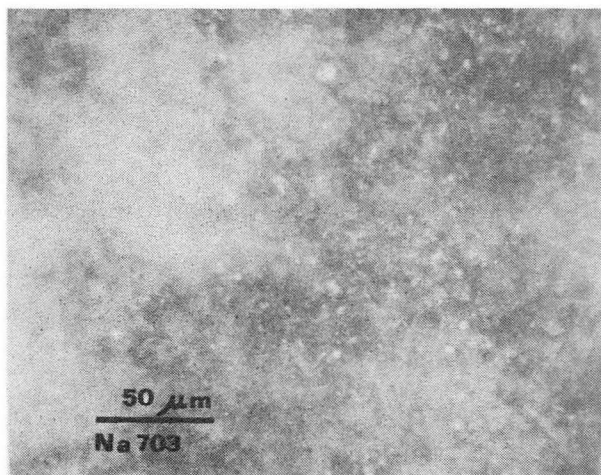
Figure 47. Higher Magnification of One of the Previous Surfaces, Optical Microscopy
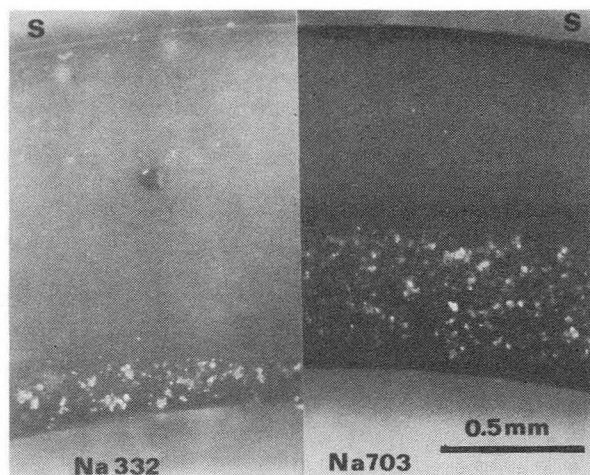
Figure 48. Polished and stained cross sections of used electrolytes, showing significant electrolyte damage that has proceeded in an uneven layer-like fashion from the sodium/electrolyte interface. The total amount of charge transfer experienced by these tubes has been indicated. current density was approximately 100 mA/cm^2

observation is shown in Figure 48. In these polished and stained cross-sections it is clearly shown that significant electrolyte damage has occurred in an uneven layer-like fashion from the sodium/electrolyte interface. At 703 Ahcm^{-2} this layer of degradation has progressed through about one-third of the tube wall. The white, spotty reflections were found from their focussing behavior in the optical microscope to be subsurface. They were found to be microfractures caused by internal sodium deposition. Evidence supporting this description of this mode of degradation is presented in Figures 49 and 50. Figure 49a is a high-voltage transmission electron micrograph of a thick foil prepared by ion milling from the degraded region of an electrolyte subjected to 332 Ahcm^{-2} of charge transfer. The arrows indicate where sodium metal appears to have deposited. The deposition occurred at some grain boundaries, as well as at some grain triple junctions. Interestingly, analytical scanning transmission electron microscopy on degraded regions such as this showed that the degraded triple junctions contained silicon as well, Figure 49b. It therefore appears that grain boundaries, as well as integranular phases, are active in the Mode II degradation. Figure 50 shows a microfracture area, observed in a thick foil with a 650 kV transmission electron microscope where excess sodium as well as
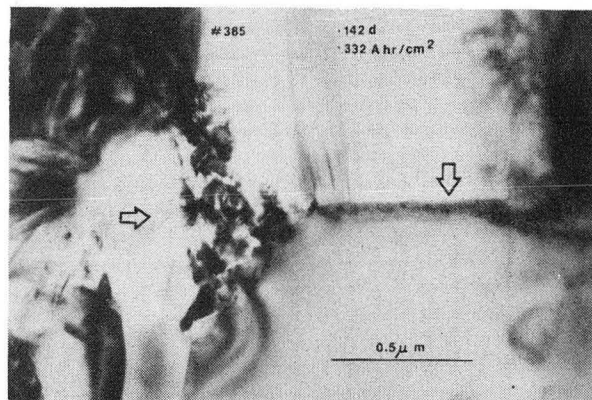
Figure 49. (a) Electron micrograph of a thick foil from the degraded region of an electrolyte subjected to 332 A hr/cm^2 of charge transfer. The arrow indicates where sodium metal appears to have deposited. (b) Scanning transmission electron microscope identification of the sodium metal. Silicon appears to be associated with this particular sodium deposit as well.
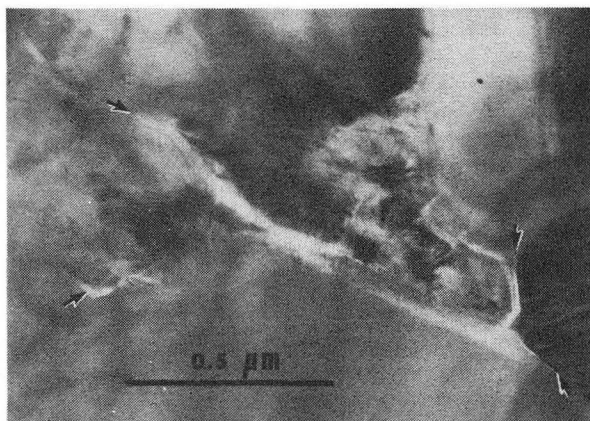
Figure 50. Microfractured area, observed in a thick foil in a 650 kV transmission electron microscope, where excess sodium is present and where the silicon was detected with the analytical scanning transmission electron microscope.

silicon was detected with the analytical scanning transmission electron microscope.

This slow Mode II sodium penetration cannot be accounted for by the Mode I Poiseuille pressure arguments. Indeed, Mode I degradation leads invariably to rapid crack propagation. Instead, we propose that the Mode II degradation involves electron conduction from the sodium/beta alumina interface followed by electron-Na$^+$ recombination in the bulk of the electrolyte. The band gap for beta aluminas is probably as high as 9 eV, and the intrinsic electronic conductivity is negligibly small at cell operating temperatures. Electrons may be injected from the Na/electrolyte interface at sufficient electric fields. However, the field distance must be many times larger than the band gap. For the sodium/sulfur cells applied electric fields over the electrolyte are on the order of 10 V/cm and are clearly insufficient to permit direct free electron injection. Instead, the observation of internal sodium formation implies that a process has occurred that has increased the electronic conductivity over its intrinsic value. The chemical coloration is, in fact, such a process. The recombination of electrons and sodium ions in the bulk can only lead to local electrolyte microfracture if it is driven in some way by the applied voltage or the current during cell charging. A driving force for internal sodium formation can result, however, only when a gradient in electronic transport number is present or, in other words, when the electrolyte is not fully equilibrated with the electrodes. The increasing coloration that can be observed indicates that the electrolytes are indeed not in equilibrium with the electrodes, even after prolonged cell operation. The Mode II mechanism proposed here is less likely to operate in thin walled electrolytes cycled in Na/Na cells: the transport number gradient should be minimal. This would also imply that the Mode II degradation involves in some way the polarization phenomena and condition of the sulphur electrode during cell operation. Microstructural and current density heterogeneities, such as the ones described by De Jonghe (2) should play a role in determining where the sodium would be nucleated.

Mode I Degradation. Mode I flaws were also observed in cycled electrolytes. An example is shown in Figure 51. It could not be determined at which point of the cycling life this Mode I crack had formed. It is possible that the micro-cracking associated with Mode II failure might actually have initiated the Mode I failure. It is interesting to note that the Mode I crack shown in Figure 51 did not remain perpendicular to the tube walls. We have attributed this
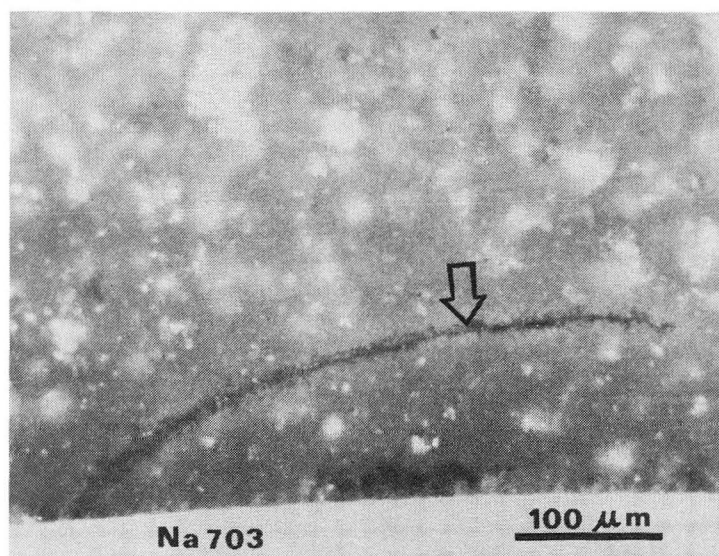
Figure 51. Mode I Flaws Observed in Cycled Electrolyte.

deflection to a basic instability in the Mode I geometry: a deflected crack is more effectively current-fed. This deflection can clearly lead to spalling of the electrolyte surfaces. Similar crack deflections were described in our accelerated sodium/sodium testing of electrolyte tubes at 300°C.

Sulfur Side

The sulfur sides of the electrolytes tested by the General Electric Company showed also signs of degradation. A micrograph comparing the four examined electrolytes is shown in Figure 52. At short times, the sulfur/electrolyte surface is virtually unaffected. At long cycling times, a significant degradation occurs as is shown in Figures 52 and 53. Figure 53 clearly shows the imprinting effect that has been reported by other workers as well. The light and dark regions in the electrolyte surface reflect the macrostructure of the graphite filter that was used to facilitate current extraction from the positive sulfur electrode. The decoration of these surfaces, with the method described earlier, revealed the presence of surface cracks, Figure 54. A cross section of the electrolyte at the positive electrode is shown in Figure 55. Again a band of degradation is observed after extensive charge transfer. This layer appears quite nonuniform at low charge transfer, but is fully established
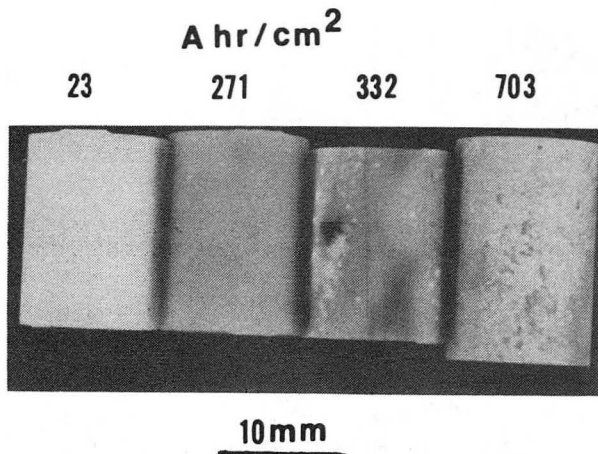
Figure 52. Comparison of the Sulfur Contact Surfaces on the Four Electrolytes Subjected to the Charge Transfers as Indicated
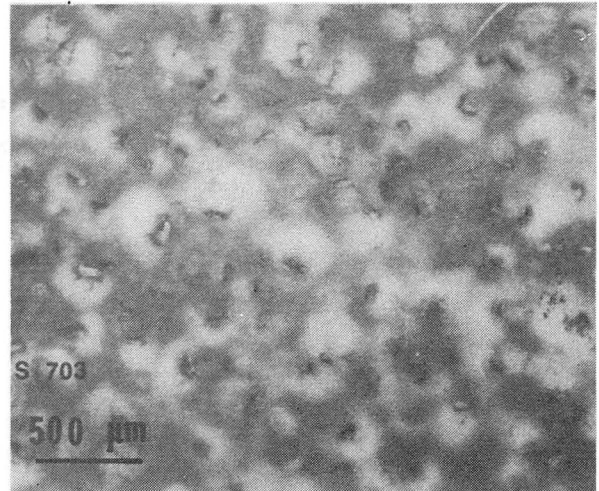
Figure 53. Imprinting Effect Associated with the Sulfur Side Degradation
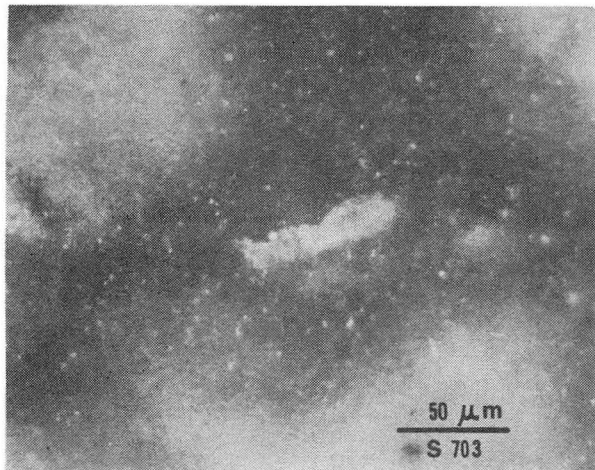
Figure 54. High magnification optical micrograph of the sulfur side of the used electrolyte. Surface cracks associated with the imprinting pattern are revealed.
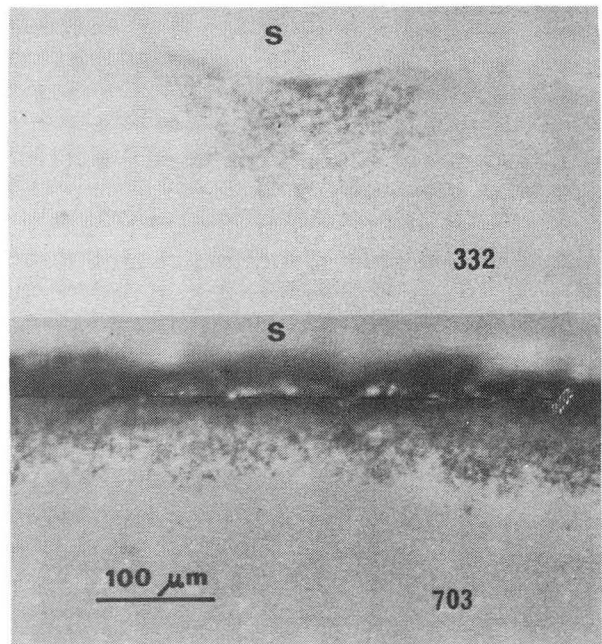
Figure 55. Cross section of the electrolyte at the positive electrode interface. The band of degradation is observed after extensive charge transfer.

after 703 A hrs/cm^2 in these samples. At present, this degradation is less well understood. The indications are again that sodium deposition has occurred. This highly unusual situation would require a positive interface to act as a pseudo-cathode during part of the charge or discharge cycle. It might be postulated that such a circumstance could arise during charging when a significant chemical polarization layer had developed in the sulfur electrode during the previous discharge cycle. Upon charging, such a chemical polarization layer containing sodium polysulfide phases could itself act as an electrolyte causing the electrolyte surface to be at a cathodic potential with respect to the graphite fibers. To form sodium metal, electrons would have to be supplied through the electrolyte. These processes are only possible after some electronic conductivity has developed in the electrolyte itself.

Some specimens were also examined in the scanning Auger microscope. This made it possible to determine that carbon and sulfur were present in the bulk of the degraded electrolyte tubes near the sulfur/beta alumina interface. Specimens observed in the microscope were fractured in situ in the Auger microscope to preclude the possibility of contamination during sample preparations. Figure 56 shows a scan taken from a fractured specimen in a region near the sulfur/electrolyte interface with a carbon and a sulfur peaks marked. Silicon was
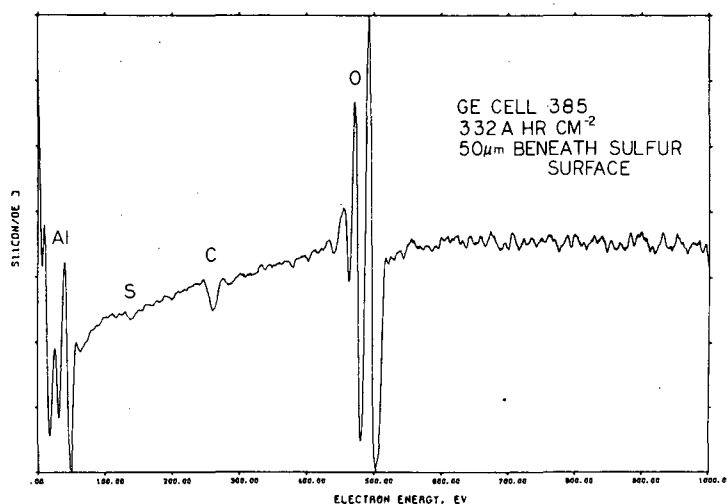
Figure 56. Auger microscope scan from a fractured
specimen of used electrolyte in the region near
the sulfur/electrolyte interface. The carbon and
the sulfur peaks are marked.

another element which was detected frequently in the G.E. electrolyte, but its distribution appeared to be irregular. It had already been observed with the scanning transmission electron microscope. The significant amount of carbon found near the sulfur surface cannot be accounted for by contamination. If there is a sodium or sodium hydroxide filled crack network below the sulfur/beta alumina surface after exposure to air, then reaction with carbon dioxide might have brought about the carbon. This should happen at the sodium surface as well. However, the carbon peaks near the sodium surface were always much weaker indicating that the carbon might have come from the graphite filler. Sodium present near the sulfur side, being formed under unusual circumstances, should be expected at some point in the cycling of the cell to react with the poly-sulfides. This could account for the presence of sulfur penetration in the solid electrolyte. The sulfur peak was smaller and sometimes disappeared altogether when a beam with a 0.1 μm diameter was positioned on transgranular fracture areas. This suggests that attack at the sulfur surface is mainly a grain boundary phenomenon.

The distribution of sodium could not be obtained from the Auger analysis since the ion is too mobile.

The sulfur side degradation of the electrolyte has to be studied much more carefully before a definite conclusion can be drawn about its origin and its significance in the sodium/sulfur cell operation. It does, however, suggest that polarization phenomena may occur at the sodium/polysulfide interface.

Section 4

DISCUSSIONS AND INTERPRETATIONS

MODE I FAILURE INITIATION

The degradation of solid electrolytes during the cell operation has received
varying degrees of attention during the beta battery cell development. In the
initial stages, significant efforts went into improvement of the solid
electrolytes so that their failures due to current passage were minimized.
Attention then turned to the seal areas in the cell where it was found that
fracture or other types of degradation often initiated. As the quality of the
seals improved, and the cell life increased significantly, it appeared to be
necessary to focus the attention once more on the breakdown and degradation of
the solid electrolytes. This experience clearly indicates that the development
of the beta battery should continue on a broad basis. To bring the average cell
life to the required 5 or 10 years lifetime, all aspects of the cell deserve
further attention. Of particular importance is whether the degradation phenom-
ena occurring in the solid electrolyte itself over a time span of several years
have put an intrinsic limit on the cell life. It is, therefore, particularly
important to understand the mechanisms by which solid electrolytes fail, in
order to understand which cell construction and cell operation parameters need
to be modified in order to suppress the degradation mechanisms.

The Mode I degradation was first discussed by Armstrong et al. ($\underline{8}$) and has been
examined in more detail by a number of authors ($\underline{9},\underline{14}$-$\underline{16}$). This degradation
involves the propagation of a sodium-filled crack driven by a cathodic deposi-
tion mechanism. In general, a significant threshold current density needs to be
exceeded before the rapid Mode I fracture-degradation is initiated. Once a
critical condition has been exceeded, propagation is rapid. The stresses arise
from the Poiseuille pressure gradient generated by the flow of sodium out of the
crack. This pressure will generate a stress intensity K_I at a crack tip.
When this stress intensity exceeds the critical stress intensity, K_{IC}, the
crack will propagate. To calculate explicitly the current flowing into the

crack requires assuming a specific crack geometry. As was discussed in this report, this crack geometry may be complicated and frequently crack branching may be observed. However, for the purpose of the calculation of initiation current density thresholds, the assumption that a single small, sodium filled crack is the active nucleus, appears to be plausible.

The exact calculation of the local cathodic deposition rates along the crack tip and faces is a complex problem. The first approach is a solution of Laplace's equation for a particular crack geometry in a perfectly isotropic dielectric. This yields the primary current distribution. However, the situation becomes more complicated when the flaw is actually carrying current. The Poiseuille pressures that are generated will in turn generate a counter EMF, ΔE, at the interface of an approximate magnitude of $\Delta E = -V_0 P/F$, where V_0 = the molar volume of sodium, P is the local pressure at the crack face, and F is Faraday's constant. This problem has been discussed in some detail by Brennan (16). Brennan also discussed the importance of the electrolyte–electrode interface charge transfer resistance on the critical current densities. These overvoltages can be significant in crack areas where large local pressures or large local current densities are calculated. The generated overvoltages act to decrease the magnitude of current focusing on the cracked tip. Brennan's analysis yields a good approximation of the secondary current distribution for the ideal crack. The problem is analogous to that of dendritic growth during cathodic plating and to other electrode deposition problems such as the one discussed by Kasper (17). The same considerations should be of significance in the calculation of the electrode current inhomogeneities such as those recently reported by Virkar et al. (15).

In the first treatment of the Mode I breakdown problem, by Armstrong et al., (18) the electrolyte was modeled as a parallel sided slab with a sodium–filled flaw extending perpendicular to the sodium/electrolyte interface. The flow is then considered along the radii of a hemispherically capped cylinder near the crack tip. The current flowing into the flaw is obtained by assuming the sodium metal to be at the same electrical potential everywhere in calculating an effective resistance around the crack tip. The approximate treatment gives the qualitative result that the crack growth velocity is proportional to the crack length and the average current density in the slab, but it does not make use of the critical fracture concept, and does not indicate a threshold current density

below which degradation of this type will not occur.

A more refined treatment is given by Shetty et al., (18) in which the crack shape is determined using elasticity theory such that its shape is self consistent with the pressure generated due to the viscous flow of the sodium within the crack. Crack profile pressure distribution is then determined by an iterative calculation to give the self-consistent results. The finding is that the profile changes little after the first iteration, given by approximately flat, parallel sided crack with rounded tip and uniform pressure gradient along the crack. By incorporating the critical fracture concept together with the linear pressure profile, large current densities are calculated to be necessary for crack extension. The current densities are on the order of about 1500 A/cm^2 for an initial flaw length of 25 μm in beta" alumina. This is about a factor of 10^4 larger than the typical average current densities that are observed for the initiation of rapid breakdown by Mode I.

A more basic calculation is given here for the current focusing and fracture problem, in that it calculates directly the primary current density distribution and sodium pressure along that crack. Some simplification in the analysis is achieved by using an elliptical-cylindrical crack shape. In what follows, we consider in detail the current flow into the sodium filled crack and the resulting Poiseuille pressure distribution and its effect on K_I. We do not take into consideration the secondary current distribution. The present calculation can therefore be considered as an upper bound to the stress intensity that is generated at the crack tip, since all other effects tend to decrease the current focusing. This further refinement of the current focusing problem leads to a critical current density that is even higher than the ones calculated in the more approximate treatments.

Current Focusing-Sodium Flow Velocity

The calculation is performed for a crack of the elliptic-cylindrical shape, as shown in Figure 57. The equation $\nabla^2\phi = 0$ is readily solved in elliptic-cylindrical coordinates in terms of elementary functions (19) and it remains only to tailor the boundary conditions to fit the present problem to determine the particular solution. The coordinate system and boundary conditions, are indicated in Figure 58. The elliptic-cylindrical coordinates are defined by
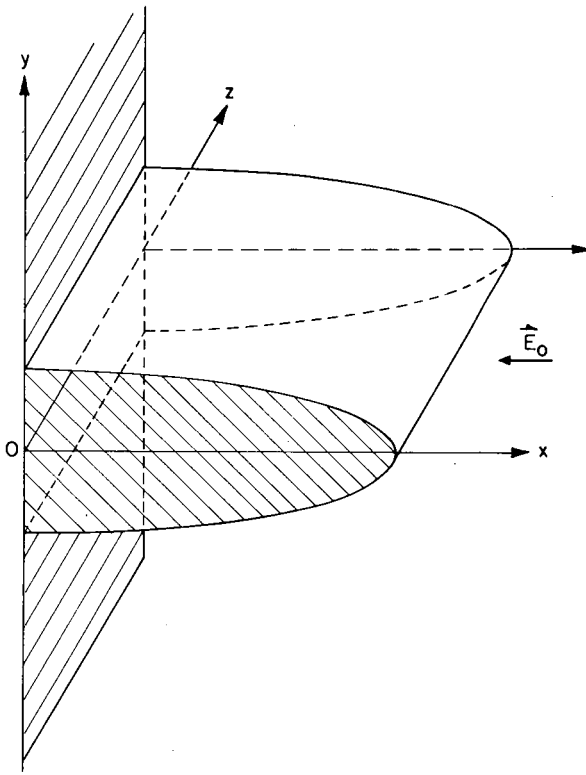
Figure 57. Crack Geometry and Elliptic-Cylindrical Coordinates
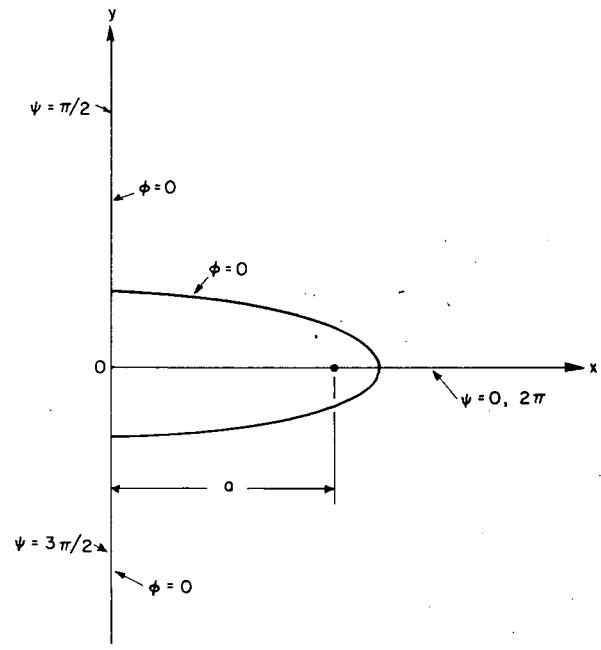
Figure 58. Coordinate Systems and Boundary Conditions for the Theoretical Calculations of the Current Focusing

$$x = a\cosh\cdot\eta \ \cos \ \psi$$
$$y = a \ \sinh\cdot\eta \ \sin \ \psi \qquad\qquad\qquad (4\text{-}1)$$
$$z = z$$

The crack parameters of length, 1, and one-half of the crack opening displacement, r, are given by

$$1 = a \ \cosh \ \eta_0$$

$$r = a \ \sinh \ \eta_0 \qquad\qquad\qquad (4\text{-}2)$$

The potential is chosen to satisfy the uniform field condition at infinity $\phi = -E_\infty(X)$, while at the sodium/electrolyte interface $\phi = 0$. The potential inside the electrolyte is then found to be:

4-4

$$\phi = \frac{E_\infty \, a \, \cos\psi}{\cosh\eta_0 - \sinh\eta_0} (\cosh\eta_0 \cdot \sinh\eta - \sinh\eta_0 \cdot \cosh\eta) \qquad (4\text{-}3)$$

The field is obtained from $E = -\nabla\phi$ in elliptic-cylindrical coordinates. The current density flowing through the surface of the crack ($\eta = \eta_0$) is

$$j = \frac{j_\infty \cos\eta \, (\cosh\eta_0 + \sinh\eta_0)}{(\cosh^2\eta_0 - \cosh\psi^2)^{1/2}} \, . \qquad (4\text{-}4)$$

where $j_\infty = \sigma E_\infty$ and σ = electrolyte specific conductivity.

The current density at the tip ($\psi = 0$) for a narrow crack ($r/l \ll 1$) is

$$j_{max} = j_\infty(1 + \coth\eta_0)$$

$$j_\infty l/r \qquad (4\text{-}5)$$

This value is a factor of two smaller than the one obtained by the approximate treatments of Richman and Tennenhouse (14).

From the current density distribution, the total sodium flux versus distance along the crack can be found, leading to an average flow velocity that appears to be independent of distance along the crack. This is probably an artifact of this crack geometry and simplifies the calculation. The current contribution per unit width, w, along z for an element of arc along the crack surface is

$$\frac{di(\psi)}{w} = 2j(\psi) \, dS \qquad (4\text{-}6)$$

where $dS = a \, (\cosh\eta^2 - \cos\psi_0^2)^{1/2} \, d\psi$.

The factor of 2 arises from the fact that current is fed in from both sides of the crack. Substituting $j(\psi)$ from Eq. (4-4) and integrating gives:

$$i(\psi) = 2j_\infty a(\cosh\eta_0 + \sinh\eta_0) \int_0^\psi \cos\, d\psi$$

or

$$i(\psi)/w = 2j_\infty a(\cosh \eta_0 + \sinh \eta_0) \sin \psi \qquad (4\text{-}7)$$

the total current into the crack ($\psi = \pi/2$) per unit width is approximately $2j_\infty a$, which compares well with the estimate of Richman and Tennenhouse (14). The flow velocity is related to the ratio of the flux through a cross section of the crack to the cross sectional area $i(\psi)/2xy(\psi)$. This average flux $\bar{j}$ is given by

$$\bar{j} = \frac{j_\infty(\cosh \eta_0 + \sinh \eta_0)}{\sinh \eta_0} \qquad (4\text{-}8)$$

The flow velocity for sodium, V, is determined from the relation $j = nev$ where n is the atom number density of liquid sodium and e is the sodium ionic charge. Thus

$$\bar{v} = v_\infty(1 + \coth \eta_0) \qquad (4\text{-}9)$$

where $v_\infty = j_\infty/ne$. Thus, the velocity v is independent of position along the crack.

Flow Pressure and Fracture Mechanics of Crack

We approach the flow pressure by assuming Poiseuille type viscous flow using the formula for flow between parallel plates of spacing 2h

$$\frac{dP}{dx} = \frac{-3\bar{v}}{h^2} \tau \quad , \qquad (4\text{-}10)$$

where $\bar{v}$ is the average flow velocity and τ is the viscosity. This assumption will be in reasonable agreement with the present geometry away from the tip of a long, narrow crack where the walls are almost parallel. In the high curvature region at the tip of flow will be more nearly perpendicular to the walls. The assumption [that $\bar{v}$ is given by Eq. (4-9) up to the crack tip] should thus overestimate the pressure gradient near the tip, giving an upper bound on the pressure. The gradient is given by

$$\frac{dP}{dx} = \frac{-3\,\bar{v}}{y^2}\,\tau = \frac{-3\,\bar{v}\,\tau}{a^2\sinh^2_0\eta\,\sin^2\psi} = \frac{-3\,\bar{v}\,\tau}{r^2(1 - x^2/l^2)} \tag{4-11}$$

Assuming $P = 0$ at $x = 0$, we integrate to find $P(x)$

$$P(x) = P_0\tanh(x/l) \tag{4-12}$$

where $P_0 = 3\,\tau\,vl/r^2$, which is the pressure head developed along a parallel sided channel of spacing $2r$ and is the pressure head value of Virkar et al. ([18]). The two pressure distributions are compared in Figure 59.

In terms of a fracture mechanics approach, K_I must be evaluated for this internally loaded crack. It is given for an internally loaded edge crack ([20]) by

$$K_I = \frac{2}{\pi}\int_0^1 \frac{[1 + f(x/l)]\,l^{1/2}\,P(x)\,dx}{\sqrt{l^2 - x^2}} \tag{4-13}$$

ELLIPTICAL CRACK PROFILE

PRESSURE DUE TO CALCULATED CURRENT DISTRIBUTION

$P/P_0 = \text{TAN H}^{-1}\, x/l$

$P/P_0 = x/l$
SHETTY et al.
(1st APPROXIMATION)

PRESSURE DISTRIBUTION
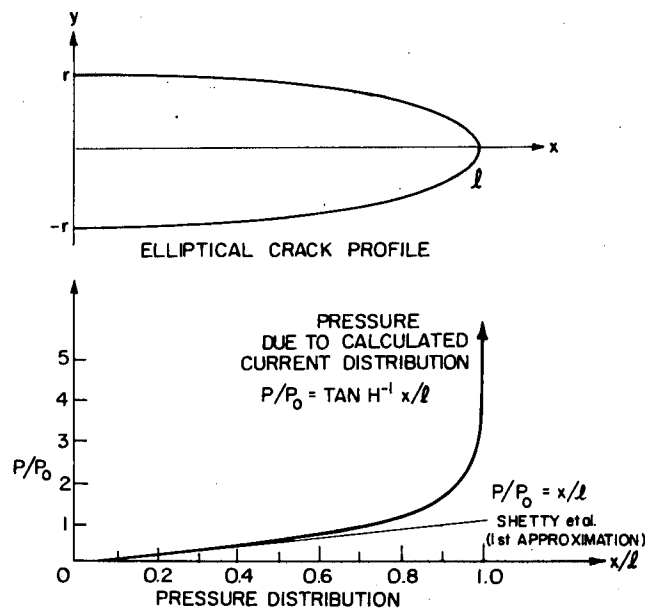
Figure 59. Comparison of the Calculated Pressure Distribution Inside the Crack

with $f(u) = (1 - u)(0.2945 - 0.3912u^2 + 0.7685\ u^4 - 0.9942u^6 + 0.5094u^8)$. Substitution of $P(x)$ from Eq. (4-12) reduces the problem to evaluating a series of convergent integrals of the form

$$\int_0^1 q^n (1 - q^2)^{-1/2} \ln\left(\frac{1 + q}{1 - q}\right) dq$$

which are transformed by substituting $y = \ln[(1 + q)(1 - q)]$ into

$$\frac{1}{2}\int_0^\infty \frac{y\ \tanh^n(y/2)\ dy}{\cosh(y/2)}$$

These integrals can be approximated numerically using Simpson's rule. The result (for r/l small) is

$$K_I = \frac{3.783\ l^{1/2}P_o}{\pi}$$

or

$$K_I = \frac{11.35}{\pi}\ \tau(1/r)^3\ l^{-1/2}\ v_\infty \tag{4-14}$$

Some results from fracture mechanics on the relation of crack displacement to length in a generalized crack geometry (21) may be used to eliminate r from Eq. (14). Fictitious forces P are applied on opposite sides of the crack at the crack opening. The new stress intensity factor becomes

$$K_I' = K_I + P/\sqrt{\pi l} \tag{4-15}$$

The stored strain energy is

$$\bar{U}_e = \int_0^l G\, dl = \int_0^l \frac{K_I'^2}{E'}\ dl = \frac{1}{E'}\int_0^l (K_I + P/\sqrt{\pi l})^2\ dl \tag{4-16}$$

The displacement is found by taking the derivative at $P = 0$

$$r = \left(\frac{\partial \bar{U}_e}{\partial P}\right)_{P=0} = \frac{2}{E'}\int_0^l K_I/\sqrt{\pi l}\ dl \tag{4-17}$$

Substituting from K_I from Eq. (4-10), self-consistency requires that

$$r = (4k/3)^{1/4} l^{3/4} \qquad\qquad (4\text{-}18)$$

where

$$k = \frac{2}{E'} \ \frac{11.35}{\pi^{3/2}} \ \tau v_\infty$$

This gives

$$K_I = 1.35 \ E'^{3/4} \ (\tau v_\infty l)^{1/4} \qquad\qquad (4\text{-}18a)$$

or

$$K_I = 1.35 \ E'^{3/4} (\tau/ne)^{1/4} \ (j_\infty l)^{1/4} \qquad\qquad (18b)$$

Some typical values of the crack parameters are shown in Table III. The value constants used are $E' = 10^5$ MPa, $\tau = 0.34$ centipoise for sodium at 300°C, ne = 4.2×10^9 coul/m^3. As can be seen the critical current densities for cracks of reasonable length are very high compared to the typical values that are observed for electrolyte failure. These values are comparable with those obtained by Shetty et al. (18)

Current Enhancement Around a Blocking Region

The problem of current distribution around a blocking layer in a solid electrolyte has been described by Virkar et al. (15) using a mechanical analog of the current flow problem. It may also be treated like the previously discussed example by choosing a suitable geometry in which Laplace's equation may be solved in order to determine the current density directly. In this case an example of a blocking layer would be a portion of the electrolyte/sodium interface which is non-conducting, such as a non-wetted region or an unfavorably oriented plate-like crystallite. An elliptic-cylindrical geometry for the insulating barrier is again used and Laplace's equation is solved in elliptic-cylindrical coordinates. The flaw geometry, boundary conditions, and current density along the electrolyte/metal interface away from the platelet are indicated in Figure 60. The potential which satisfies the boundary condition is

TABLE III

CALCULATED VALUES OF 1, j_∞, AND K_I/K_{IC}

1(μm)	j_∞(A/cm^2)	H_I/K_{IC}
10	0.1	0.025
	10	0.08
	1000	0.25
100	0.1	0.045
	10	0.14
	1000	0.45
1000	0.1	0.08
	10	0.25
	1000	0.8

$j_\infty + K_I^4 \, E'^3 \, ne/(3.32 \, \tau \, 1)$

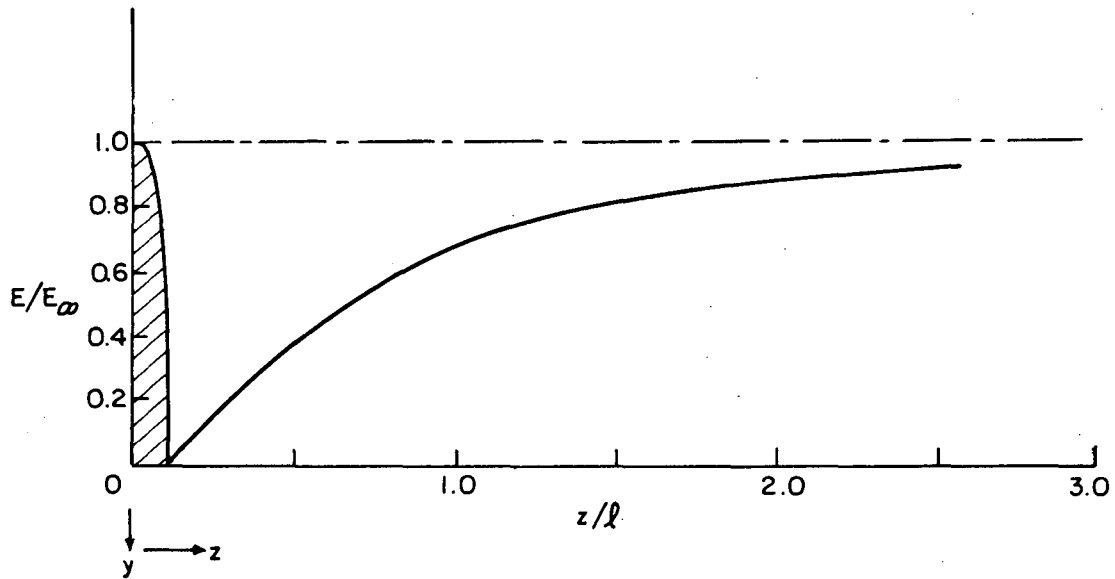$K_{IC} \simeq 1.6$ MPa m$^{1/2}$, Shetty et al. [18]

Figure 60. Flaw Geometry, Boundary Conditions and Current Density along the Electrolyte/Metal Interface Away from the Blocking Platelet in the Electrolyte Surface

$$\phi = \frac{E_\infty \, a \, \sin\psi(\cosh \eta_0 \cosh \eta - \sinh \eta_0 \sinh \eta)}{-1(\cosh \eta_0 - \sinh \eta_0)} \tag{4-19}$$

from which the electric field and current density in the electrolyte are determined directly. The current density enhancement at the edge of the platelet, $\eta = \eta_0$; $\psi = 0, \pi$ is

$$j_{max} = \frac{j_\infty(\cosh \eta_0 + \sinh \eta_0)}{\sqrt{\cosh^2 \eta_0 - 1}} = j_\infty(\coth \eta_0 + 1) \simeq j_\infty l/r \tag{4-20}$$

This current density enhancement around the edge of the platelet is a factor of two smaller than obtained by Virkar et al. (15) from the mechanical analog of the problem.

It is necessary to know the spatial extent of the zone of enhanced current density around the platelet. This allows an estimate of the increased current focusing experienced by an initial flaw situated at the edge of a platelet. From the relation of current density to position along the electrolyte/metal electrode interface the maximum current density is found to occur at the platelet edge and to decrease smoothly to the value j_∞ far from the platelet. Let us now take the current density to be uniform in the current enhanced region, instead of decreasing, with a value of $j_{max} \simeq j_\infty l/r$. Let us also take the current density to be uniform outside the enhanced region, with a value of j_∞. Since the boundary condition of uniform current density of magnitude j_∞ at large y imposes a definite total current, the conservation of current (Kirchoff's Law) determines the width, R, of the high field or high current region. The total current in that region, $j_{max}Rw$, must be, to a first approximation, $j_\infty lw$, for $r/l \ll 1$, which would be half the current flowing through the platelet area if the blocking platelet were removed. The current flowing around the platelet is in a sense a "displacement" current. Equating the current in the enhanced zone with the total displaced current gives a zone of width $j_\infty l/j_{max}$, or r. Thus, for $r/l \ll 1$ and large current density enhancement, the zone size is also very small compared to the length of the platelet. A somewhat more exact argument, which gives the same basic result can be made by finding the point of intersection of the tangents to the integrated current versus position curve, Figure 61. The tangents to the curve are constructed at the platelet edge and at infinity, on the interface.
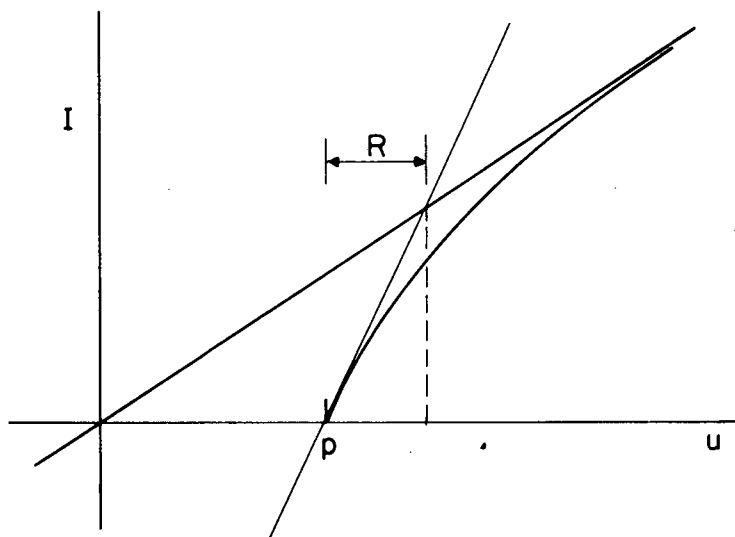
Figure 61. Determination of the High Current
Density Zone Size by Means of Intersecting Tangent
Constructions

Table IV gives the values of j_{crit} for several assumed initial flaw lengths, L_c, and the approximate zone size, R, of the enhanced current density region near the platelet edge where the current density exceeds j_{crit}. The insulating platelet size was taken to be 1 cm, r/l was 10^{-7}, and j_∞ was 1 A/cm^2. The zone dimension R was estimated from a calculation of j_y.

TABLE IV

MICROCRACK SIZE, L_C, CRITICAL CURRENT DENSITY, j_{crit}, AND CRITICAL
ZONE SIZE, R, FOR j_∞ = 1A/cm^2, 1 = 1 cm, AND R/1 = 10^{-7}

L_c (μm)	j_{crit} (A/cm^2)	R (cm)
10	2.5×10^5	8×10^{-12}
100	2.5×10^4	8×10^{-10}
1000	2.5×10^3	8×10^{-8}

$$j_y = j_\infty \frac{\coth \eta \coth \eta_0 - 1}{\coth \eta_0 - 1}$$

(4-21)

where j_y is the current density ahead of the plate edge normal to the x-z plane. It could also be obtained from the approximation of Eq. (4-18) since $j_y/j_\infty \simeq (1/2R)^{1/2}$, for $r/l < (2R/l)^{1/2} \ll 1$.

It is seen that the current enhancement zones are many orders of magnitude too small, or that the experimentally observed critical currents of a few A/cm^2 are many orders of magnitude lower than the calculated ones.

Effective K_{IC} for Initiation of Degradation

The results indicate that the Mode I mechanism needs to be modified in order to account for the large discrepancy that exists between calculated and observed critical current densities. It is difficult to envisage that an anomalously high viscosity, e.g., due to impurities or to geometrical restrictions in the capillary channel of sodium, could account for the discrepancy factor of about 10^5; rather, the results indicate that the effective critical stress intensity factor, K_{IC}^{eff} is not the same as the one that is appropriate for mechanical testing, K_{IC}. The results require that K_{IC}^{eff} is about equal to about $0.06\ K_{IC}$, since j_{crit} is proportional to $K_{IC}^{1/4}$. Processes are, therefore, occurring at the crack tip that significantly lower K_{IC} from its mechanical value. One such process is the local injection of electrons from the sharp, sodium filled crack tip, even at modest applied voltages. The field at the crack tips, E_0 is about $E_0 \simeq E_\infty/r$. From the observation of De Jonghe et al. (22), it is clear that r, the crack tip radius, can be as low as 10Å. E_0 can thus easily reach local values of 10^5 V/cm (for $E_\infty = 10$ V/cm and $L_C = $ to 10 micrometers) which may lead to profuse but localized field injection of electrons. This process would introduce significant electronic conductivity in the ceramic in the immediate vicinity of the crack tip, leading to sodium deposition under pressure just ahead of the crack tip. This could strongly affect the stress intensity factor leading to crack growth at some critical field that is reached well below the microscopic current density at which the mechanical stress intensity factor K_I would exceed the critical stress intensity factor, K_{IC}.

The degree to which local injection is possible will depend on where the

conduction band edge of the electrolyte is located with respect to the Fermi level. In this report, evidence has been given that the electrolyte is partly reduced by contact with sodium leading to oxygen vacancy formation compensated by two electrons. The oxygen vacancy electron complex is likely to be a shallow donor, i.e., it will raise the Fermi level close to the conduction band edge at the electrolyte/sodium interface. This then would permit relatively easy local injection with the resulting sodium formation and lowering of K_{IC}. It is possible, however, that the viscosity effect would dominate K_{IC} when the sodium metal is solid. In general, we thus expect a combination of Poiseuille pressure and electron injection effects to determine K_{IC}^{eff}. Since the sodium metal ahead of the crack tip forms at the rate that is limited by the rate of supply of the ions by conduction, a time dependence on K_{IC}^{eff} should be expected, especially at low temperatures: if the rate of formation of Na ahead of the crack is slowed, an apparently higher K_{IC}^{eff} should be observed at short times.

MODE II DEGRADATION

We must now consider the consequences of the electronic conductivity that is introduced by the chemical coloration process. When this coloration occurs, proceeding from the sodium electrode, transport number gradients will be maintained through the electrolyte, both for electrons and for ions. Since charge cannot accumulate inside the electrolyte, a process must occur that raises the chemical potential of the ions until the electronic and ionic current divergence has been eliminated. This is equivalent to raising the chemical potential of sodium metal inside the electrolyte. An upper bound to the sodium metal chemical potential distribution can then be calculated under the assumption that the gradients in transport numbers are invariant during electrolysis. At sufficiently high applied changing voltages the chemical potential of sodium inside the electrolyte should then actually rise above that of the sodium electrode. This can produce the internal formation of sodium, under pressure, at preferred nucleation sites, such as grain boundaries or preexisting internal flaws, by the process of internal electrolysis, i.e., electron-ion recombination. When used in a beta battery, the counter EMF over the electrolyte will tend to lower the local chemical potential in the electrolyte, while the internal electrolysis will tend to raise it. A critical applied voltage will therefore have to be exceeded during cell charging depending on the counter EMF over the electrolyte itself. This counter EMF is decreased by the polarization phenomena at the positive electrode/electrolyte interface and by the condition

of the sulfur electrode itself. When polarization at the sulfur/electrolyte interface becomes high, decreasing the counter EMF over the electrolyte, we expect the critical applied voltage to be lowered. The full details of the calculation will be developed in the next program year. Preliminary calculations have indicated that the critical over voltage for the onset of Mode II degradation is on the order of 1.5 times the counter EMF appearing over the electrolyte. If interface polarizations were absent, this would lead to the critical charging voltage of about 3 V. The results can be expressed as a critical voltage, V_{crit}, over the electrolyte itself.

One could also express them as a critical current density, I_{crit}, if the effective electrolyte resistance, σ_{eff}, is taken into account. Since $I_{crit} = V_{crit}\sigma/\ell$, where ℓ is the electrolyte wall thickness, it would follow that for constant current density charging an increased electrolyte wall thickness is unfavorable to a long cell life. Additionally, a decreased electrolyte conductivity would also adversely affect the onset of the Mode II degradation. The model for the Mode II degradation thus predicts that the following factors contributed adversely to the durability of the solid electrolytes.

1. Applied voltages in excess of 3 V.
2. Increased electrolyte thickness.
3. Increased electrolyte resistance.
4. Polarization at the sulfur/electrolyte interface.

Section 5

CONCLUSIONS AND RECOMMENDATIONS

CONCLUSIONS

● The microstructure of electrolyte tubes used in different laboratories was examined. While the presence of several types of imperfections might suggest that improvement in the tube processing is obtainable, it has not been possible to relate the observable defects to causes of electrolyte failure or degradation. From what is currently understood about electrolyte failure, it would appear that the further development of the appearance of the microstructure of the electrolyte would have little, if any effect on in-cell performance.

● A silver staining method was developed that permitted a clear and unambiguous decoration of flaws introduced during electrolyte degradation.

● An electrolytic silver decoration method was developed that permitted an estimate of the electrode current inhomogeneities caused by the unisotropic nature of the solid electrolyte. The resolution of the technique is about 1 micrometer. Local current densities were estimated to vary by a factor of about 5.

● Two types of degradation were found to occur. Mode I was the well-known failure by cracking due to Poiseuille pressures generated as a result of cathodic plating into a preexisting surface microcrack. Mode II involved the internal deposition of sodium, due to the introduction of some gradient in the electronic conductivity.

● Degradation associated with the graphite felt imprinting effect was observed on the sulfur side of electrolytes used in sodium/sulfur cells.

● A refined fracture mechanics treatment still was unable to account for the observed low critical current densities for Mode I initiation. The discrepancies are on the order of a factor of 10^5. It was concluded that local injection of electrons at the Mode I crack tip contributes very significantly to lowering K_{IC} from its mechanical value.

● Geometrical aspects were considered for the Mode I failure initiation. This led to the conclusion that grain boundaries should be favored sites for Mode I initiation. Sodium/sodium cell test results of large grain size electrolytes supported this conclusion.

- A model for the Mode II degradation was considered. Approximate considerations put the applied voltage for Mode II initiation at about 1.5 times the counter EMF over the electrolyte. This would predict that the following factors contributed adversely to electrolyte lifetime:

    1. Applied charging voltages over 3 V.
    2. High electrolyte resistance
    3. Interface polarization effects
    4. Increased electrolyte thickness.

- A number of degradation experiments were performed on single and polycrystals. These demonstrated that Mode I crack branching is profuse in the propagation stage. They also demonstrated that the sodium ion supply to a Mode I crack differs substantially from the isotropic flow assumed in the models.

- Acoustic emissions (A.E.) monitoring was found to be the most sensitive way for detecting Mode I failure initiation.

- The critical current densities for Mode I, below $100°C$ were found to vary widely. The scatter could be described by a Weibull-type distribution with a parameter of 1 to 5. A weak indication was also found in these experiments that the Mode I failure below $100°C$ related to the small grain fraction. The temperature dependence of the current density threshold was found to be about 4 kcal/mol.

- The acoustic emissions monitoring was used to test beta" electrolytes in sodium/sodium cells at $350°C$. A statistically significant lower current density threshold for Mode I initiation was found for large grain size material. The results thus did not agree with the low temperature tests. This raises a question about the validity of low temperature critical current density testing.

- At $350°C$ the average critical current density for Mode I was about 0.15 to 0.25 A/cm^2, depending on grain size. The Weibull modulus was about 1.5.

- Mode I cracks tend to deflect and run parallel to the electrolyte surfaces. This can give rise to spalling, circumferential or spiral fractures.

- Coloration of the electrolytes by sodium was studied. The results indicate unambiguously that sodium chemically reduces the electrolyte, removing oxygen. Charge compensation is electronic. This chemical coloration accounts for the gradient in electronic conductivity that makes the Mode II operation possible.

RECOMMENDATIONS FOR FUTURE RESEARCH

- The statistical nature of the Mode I failure, exhibiting a low Weibull modulus, is a potentially serious problem. Efforts should be made to establish clearly what the intrinsic scatter of

electrolyte failure is under the best control and simplest conditions. Statistical information should therefore be gathered on a large number of sodium/sodium cells of the type described in this report.

- The role of interfacial polarizations and electrode impurities, in the Mode I degradation initiation needs to be established.

- The conditions under which Mode II becomes operative needs to be studied further in theory as well as in experiments.

Development of the sodium/sulfur cell needs to continue on a broad front. Especially those factors that contribute to cell contamination need to be eliminated. Further efforts on sulfur electrode development that attempt to minimize polarization and impurity effects are necessary.

- A "standard" cell construction should be agreed upon by all sodium/sulfur developers, permitting electrochemical and lifetime measurements that are directly comparable. These cells should be intensely studied even though scale-up appears, at present, to be warranted.

- Efforts should be directed towards recording those aspects of sodium/sulfur cell operation that might contribute to early cell failures. These effects include unusual cell polarization events. The microstructure of the tested electrolytes, as revealed for example by silver staining, should be examined for those cells in which unusual polarization events were observed. A wider exchange of used electrolytes and information is therefore highly desirable.

- The degradation at the sulfur side of the electrolytes heads to be investigated in detail.

Section 6

REFERENCES

1. C. A. Worrell and B. A. W. Redfern, J. Mat. Sci. 13, 1515 (1978).

2. L. C. DeJonghe, J. Mat. Sci. 14, 33 (1979).

3. R. N. Davidge, "Mechanical Behavior of Ceramics," Cambridge Univ. Press, 1979.

4. R. W. Davidge, G. Tappin, J. R. McLaren, and G. J. May, J. Amer. Ceram. Soc. 58, 771 (1979).

5. M. W. Breiter, B. Dunn, and R. W. Powers, Electrochim. Acta 25, 613 (1980).

6. Y. Lazennec, C. Lasne, P. Margotin, J. Fally, J. Electrochem. Soc. 122, 734 (1975).

7. G. J. Tennenhouse, R. L. Ku, R. H. Richman, and T. J. Whalen, Bull. Amer. Ceram. Soc. 54, 523 (1975).

8. R. D. Armstrong, T. Dickinson, and J. Turner, Electrochim. Acta 19, 187 (1974).

9. A. V. Virkar and L. Vishanathan, J. Amer. Ceram. Soc. 62, 528 (1979).

10. J. T. Kummer, Prog. Solid State Chem. 7, 141 (1972).

11. M. S. Whittingham, J. Electrochem. Soc. 11, 1 (1971).

12. N. Weber, Energy Conversion 14, 1 (1974).

13. E. Hart, Acta Met. 5, 587 (1957).

14. R. H. Richman and G. J. Tennenhouse, J. Amer. Ceram. Soc. 58, 63 (1975).

15. A. Virkar, L. Viswanathan and P. R. Biswas, J. Mat. Sci. 15, 302 (1980).

16. M. P. J. Brennan, Electrochim. Acta 25, 621 (1980).

17. C. Kasper, Trans. Electrochem. Soc. 77, 353 (1940); 77, 365 (1940); 78, 131 (1940); 78, 147 (1940); 82, 153 (1942).

18. D. K. Shetty, A. Virkar, and R. S. Gordon, in "Fracture Mechanics of Ceramics," Vol. 4, R. Bradt and D. Hasselman, eds., Plenum Press, New York, 1978, pp. 65-66.

19. P. Moon, D. Spencer, "Field Theory for Engineers," D. Van Nostrand, Princeton, 1961.

20. G. C. Sih, "Handbook of Stress Intensity Factors," Lehigh University Press, 1973.